

# Stellar Population Astrophysics (SPA) with the TNG<sup>\*</sup>

## NLTE atmospheric parameters and abundances of giant stars in 33 Open Clusters

M. Dal Ponte<sup>1</sup>, V. D’Orazi<sup>2,1,3</sup>, A. Bragaglia<sup>4</sup>, A. R. Casey<sup>5,6,7</sup>, N. Storm<sup>8</sup>, L. Spina<sup>9,1</sup>, J. Alonso-Santiago<sup>10</sup>, G. Andreuzzi<sup>11,12</sup>, A. Frasca<sup>10</sup>, J. Kos<sup>13</sup>, S. Lucatello<sup>1</sup>, D. Romano<sup>4</sup>, A. Vallenari<sup>1</sup>, and N. Vernekar<sup>1</sup>

<sup>1</sup> INAF - Osservatorio Astronomico di Padova, vicolo dell’Osservatorio 5, 35122 Padova, Italy  
e-mail: marina.dalponte@inaf.it, valentina.dorazi@inaf.it

<sup>2</sup> Department of Physics, University of Rome Tor Vergata, via della Ricerca Scientifica 1, 00133 Rome, Italy

<sup>3</sup> Department of Astronomy & McDonald Observatory, The University of Texas at Austin, 2515 Speedway, Austin, TX 78712, USA

<sup>4</sup> INAF - Osservatorio di Astrofisica e Scienza dello Spazio di Bologna, via P. Gobetti 93/3, 40129 Bologna, Italy

<sup>5</sup> Department of Physics and Astronomy, Monash University, Clayton, VIC 3800, Australia

<sup>6</sup> ARC Centre of Excellence for All Sky Astrophysics in 3 Dimensions (ASTRO 3D), Australia

<sup>7</sup> Center for Computational Astrophysics, Flatiron Institute, 162 5th Avenue, New York, NY 10010, USA

<sup>8</sup> Max Planck Institute for Astronomy, Königstuhl 17, 69117 Heidelberg, Germany

<sup>9</sup> INAF-Osservatorio Astrofisico di Arcetri, Largo E. Fermi 5, 50125, Firenze, Italy

<sup>10</sup> INAF - Osservatorio Astrofisico di Catania, via di S. Sofia 78, I-95123, Catania, Italy

<sup>11</sup> INAF - Osservatorio Astronomico di Roma, via Frascati 33, 00178, Monte Porzio Catone, Italy

<sup>12</sup> Fundación Galileo Galilei - INAF, Rambla José Ana Fernández Pérez 7, 38712, Breña Baja, Tenerife, Spain

<sup>13</sup> Faculty of Mathematics and Physics, University of Ljubljana, Jadranska 19, 1000 Ljubljana, Slovenia

Received XX; acceptedXX

### ABSTRACT

**Context.** Open clusters serve as important tools for accurately studying the chemical evolution of the Milky Way. By combining precise chemical data from high-resolution spectra with information on their distances and ages, we can effectively uncover the processes that have shaped our Galaxy.

**Aims.** This study aims to derive non-local thermodynamic equilibrium (NLTE) atmospheric parameters and chemical abundances for approximately one hundred giant stars across 33 open clusters with near-solar metallicity. The clusters span a wide range of ages, enabling an assessment of the presence and extent of any age-related abundance gradients.

**Methods.** In the Stellar Population Astrophysics (SPA) project, we acquired new high-resolution spectra of giant stars in a sample of open clusters using the HARPS-N echelle spectrograph at the Telescopio Nazionale Galileo (TNG). We chemically characterized nine open clusters for the first time and reanalyzed previously studied SPA clusters, resulting in a consistent and homogeneous sample.

**Results.** We determined NLTE atmospheric parameters using the equivalent width method and derived NLTE chemical abundances through spectral synthesis for various elements, including  $\alpha$  elements (Mg, Si, and Ti), light odd-Z elements (Na, Al), iron-peak elements (Mn, Co, and Ni), and neutron-capture elements (Sr, Y, and Eu). Our findings are compared with the existing literature, revealing good agreement. We examine the trends of  $[X/Fe]$  versus age, confirming previous observations and the enrichment patterns predicted by nucleosynthesis processes. Positive correlations with age are present for  $\alpha$  elements such as Mg, Si, Ti, odd-Z Al, and iron-peak elements Mn, Co, Ni, and Sr, while Na and neutron-capture Y and Eu show a negative trend. This study emphasizes the significance of NLTE corrections and reinforces the utility of open clusters as tracers of Galactic chemical evolution. Furthermore, we provide a benchmark sample of NLTE abundances for upcoming open cluster surveys within large-scale projects such as 4MOST and WEAVE.

**Key words.** open clusters and associations: general – Stars: abundances – stars: evolution – Galaxy: abundances – Galaxy: disk – Galaxy: evolution

## 1. Introduction

Open clusters (OCs) are groups of stars that originate from the same molecular cloud at practically the same time, therefore, they have similar ages, kinematics, and chemical compositions. As a single stellar population, their ages and distances can be

estimated with great accuracy (Bragaglia & Tosi 2006; Bossini et al. 2019; Monteiro & Dias 2019; Cantat-Gaudin et al. 2020). OCs are ideal tracers of the structure of the Milky Way, and have long been utilized to investigate the Galactic (thin) disk and its chemo-dynamical evolution over time (e.g. Janes 1979; Sestito et al. 2008; Magrini et al. 2009; Frinchaboy et al. 2013; Netopil et al. 2016; Casamiquela et al. 2017; Spina et al. 2021). Large spectroscopic surveys such as Gaia-ESO (Gilmore et al. 2012; Randich et al. 2013, 2022), GALAH (De Silva et al. 2015), APOGEE (Majewski et al. 2017) and LAMOST (Zhao et al.

\* Based on observations made with the Italian Telescopio Nazionale Galileo (TNG) operated on the island of La Palma by the Fundación Galileo Galilei of the INAF (Istituto Nazionale di Astrofisica) at the Observatorio del Roque de los Muchachos.

2012), coupled with the high-quality data from the Gaia mission (Gaia Collaboration et al. 2016, 2023a), have significantly improved our understanding of the OC population. As a result of the Gaia mission, a large number of OCs were discovered and characterized, while many candidate clusters were expunged from the catalogs (see e.g., Cantat-Gaudin et al. 2018; Castro-Ginard et al. 2019; Liu & Pang 2019; Hao et al. 2022; Castro-Ginard et al. 2020; Hunt & Reffert 2023). In the coming years, WEAVE (Dalton et al. 2018; Jin et al. 2024) and 4MOST (de Jong et al. 2019; Lucatello et al. 2023) will observe many more clusters at low and intermediate resolution ( $R \approx 5000$  and  $20000$ ) and provide new insights on their properties. Despite this, a significant portion of OCs remain unexplored in detail, particularly in terms of their chemical composition, limiting our ability to fully use these objects to probe the Galactic disk’s chemical and dynamical evolution.

The Stellar Population Astrophysics (SPA) is an ongoing project based on a Large Programme conducted at the Telescopio Nazionale Galileo (TNG) using the HARPS-N and GIANO-B echelle spectrographs for about 70 nights from 2018 to 2021. Within SPA, we acquired high-resolution spectra of stars near the Sun, covering a broad range of ages and properties. To improve our understanding of the Milky Way’s star formation and chemical enrichment history, the program focuses on several topics, such as mapping abundance gradients, cosmic spreads, and other irregularities in the abundances and ratios of individual elements within the Galactic disk. We specifically observed a selection of open clusters by either targeting a few stars—mainly giants—in as many clusters as possible, or by focusing on a larger number of stars—primarily main sequence stars—in a smaller set of clusters. The primary goals of these observations were to determine the metallicity and detailed chemical composition across a broad sample of open clusters, taking advantage of their nature as a single stellar population. This means that even a single star can offer valuable insights into the entire cluster, though observing multiple members enhances the precision of key cluster parameters. Additionally, the project investigated how stellar properties relate to evolutionary stages, examining factors such as surface chemical variations caused by diffusion or mixing processes, as well as the evolution of stellar rotation and activity. Several papers have been published as part of the SPA project, analyzing either giant stars or main sequence stars Frasca et al. (2019); D’Orazi et al. (2020); Casali et al. (2020a); Alonso-Santiago et al. (2021); Zhang et al. (2021, 2022); Fanelli et al. (2022); Vernekar et al. (2024).

In this paper, we present a homogeneous analysis of high-resolution spectra of 95 giant stars across 33 open clusters, including nine clusters that are spectroscopically characterized for the first time by our team. Providing data for these previously understudied OCs is crucial for enhancing our understanding of the Galactic disk. We re-analyze giants from Casali et al. (2020a); Zhang et al. (2021, 2022), and Alonso-Santiago et al. (2021) and include giants from NGC 2632, which D’Orazi et al. (2020) studied in the SPA project but focused only on main sequence stars. By ensuring a homogeneous analysis of all spectra, we expand the SPA sample of open clusters. Furthermore, while the previous analyses assumed local thermodynamic equilibrium (LTE) conditions, which may not be suitable for many elements and temperature/surface gravity ranges, we derive atmospheric parameters and abundances using a non-LTE (NLTE) approach.

The structure of the paper is as follows. Section 2 presents the observations and describes the selected sample of open clusters. In Sect. 3, we outline the methods employed to determine stellar parameters and abundances. In Sect. 4 we present a com-

parison with the literature. Section 5 investigates the relationships between abundances and age gradients. Finally, Sect. 6 provides a summary of our findings and conclusions.

## 2. Observations and the cluster sample

The SPA Open Cluster program (SPA-OC) studies main-sequence and giant stars within open clusters. The main-sequence stars in SPA are primarily located in younger, closer clusters, whereas red giants are typically observed in older and more distant clusters (within about 2 kpc from the Sun). In this work, we focus on evolved stars on the red giant branch (RGB) and red clump (RC). The targets have been selected among the high-probability open cluster members based on Cantat-Gaudin et al. (2018, 2020), who relied on astrometry and photometry from Gaia Data Release 2 (DR2).

We deal here with the analysis of the optical HARPS-N spectra with resolution  $R \approx 115,000$  and spectral coverage between 3800–6900 Å (Cosentino et al. 2012). The analysis and results based on GIANO-B near-infrared spectra are presented in a series of dedicated papers, e.g. Bijavara Seshashayana et al. (2024a,b); Jian et al. (2024).

The observations discussed in this study were conducted between July 2018 and April 2023. The spectra were automatically reduced with the HARPS-N pipeline, which includes flat-field and bias corrections, wavelength calibration, extraction of 1D spectra, and corrections for barycentric motion. Exposure times varied depending on the star’s magnitude and sky conditions, and we combined the multi-exposure spectra before the analysis.

As mentioned before, our sample includes a total of 95 giant stars from 33 open clusters. Table 1 displays their names, the number of stars per cluster, and basic parameters such as age, distance, Galactocentric distance, and extinction. The table also indicates references for previous metallicity determinations based on high-resolution spectroscopy; for clusters with high-quality spectroscopy listed in Netopil et al. (2016) we do not provide the references to the original papers. Note that some of these metallicities were not available at the time of observation (see e.g., UBC 3, UBC 141, and UBC 577) and that some metallicities are based on low or intermediate resolution spectroscopy (see below).

Among the 33 open clusters discussed in this study, 20 were previously analyzed in SPA papers (Casali et al. 2020a; D’Orazi et al. 2020; Zhang et al. 2021, 2022; Alonso-Santiago et al. 2021), see references in Table 1<sup>1</sup>. Four clusters have been reported in the literature by other authors but are presented here for the first time in the context of the SPA project (see Fig. 1 and Table 1). Finally, this is the first metallicity determination based on high-resolution spectroscopy for nine OCs (NGC 6800, UBC 131, UBC 169, UBC 170, UBC 194 without metallicity values and NGC 7086, UBC 60, UBC 141, UBC 577 with values based on low-resolution LAMOST or medium-resolution Gaia-RVS spectra).

The inclusion of the 20 open clusters already studied in the SPA framework allows us to have a broader sample analyzed homogeneously and to extend the age range. These 33 open clusters in the SPA sample are generally located close to the Galactic midplane and to the Sun (average Galactocentric distance of 8.6 kpc, with  $R_{GC}$  spanning from 7 kpc to approximately 10 kpc) and have ages ranging from about 40 Myr to 4 Gyr (see Table 1).

<sup>1</sup> The cluster Collinder 350 is analyzed in both Casali et al. (2020a) and Zhang et al. (2021).

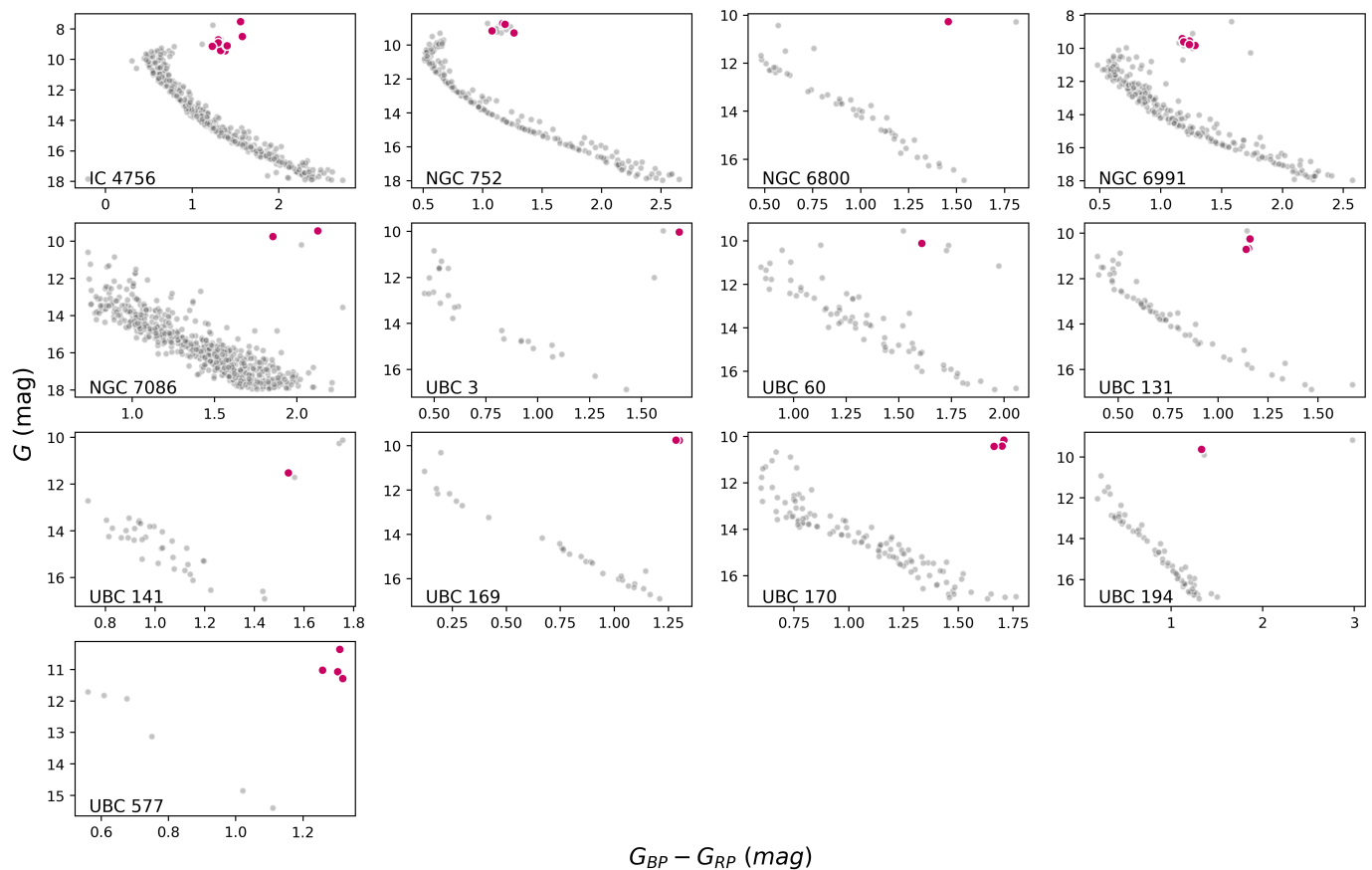


**Fig. 1.** Color-magnitude diagrams with Gaia DR3 photometric data ( $G$  vs.  $G_{BP} - G_{RP}$ ) for the subset of clusters presented in this study for the first time as part of the SPA project. The red points highlight the member stars observed by SPA.

Figure 1 presents the color-magnitude diagrams using Gaia DR3 photometric data for the 13 open clusters that have not been included in previous SPA analyses. We also provide a brief description of these clusters in the following paragraphs.

**IC 4756** - This intermediate-age cluster (about 1.3 Gyr old, according to Cantat-Gaudin et al. 2020, 970 Myr according to Bossini et al. 2019) is located very close to the Sun ( $\approx 500$  pc) at a Galactocentric distance of  $\approx 8$  kpc. Several studies have assessed its metallicity, with a few of them also investigating its detailed elemental abundances (Jacobson et al. 2007; Santos et al. 2009; Smiljanic et al. 2009; Pace et al. 2010; Ting et al. 2012; Bagdonas et al. 2018; Casamiquela et al. 2017, 2019; Ray et al. 2022; Tsantaki et al. 2023; Carbajo-Hijarrubia et al. 2024). We have eight stars in common with the existing literature, which will later be used for comparison with our results (details can be found in Sect. 4).

**NGC 752 (and Theia 1214)** - This cluster is located near the Sun and has an intermediate age—approximately 1.2 Gyr (Cantat-Gaudin et al. 2020) or 1.48 Gyr (Bossini et al. 2019). It has been extensively studied, particularly for lithium measurements, as discussed in works such as Boesgaard et al. (2022) and related references. Other metallicity and abundance studies include Sestito et al. (2004); Carrera & Pancino (2011); Reddy et al. (2012); Böcek Topcu et al. (2015); Casamiquela et al. (2017, 2019); Lum & Boesgaard (2019); Spina et al. (2021); Myers et al. (2022); Donor et al. (2020); Carbajo-Hijarrubia et al. (2024). The cluster shows signs of either dynamical or tidal dispersal (Carraro et al. 2014) and features long, asymmetric

tidal tails extending over 260 pc on the sky (Bhattacharya et al. 2021; Boffin et al. 2022; Kos 2024). In addition, Theia 1214, one of the strings discovered by Kounkel & Covey (2019), is likely associated with NGC 752. We added to the sample two stars that are part of Theia 1214 according to Kounkel & Covey (2019). However, in this work, we consider them as members of NGC 752. In total, we have five stars, where the three stars observed in the main body of the cluster are in common with the literature.

**NGC 6800** - Located at approximately 8 kpc and with an age of around 400 Myr (Cantat-Gaudin et al. 2020 or 345 Myr, Bossini et al. 2019), this OC has not yet been chemically characterized in the literature.

**NGC 6991** - It has an intermediate age of roughly 1.5 Gyr and is located about 580 pc from the Sun at a Galactocentric distance of approximately 8.4 kpc. Its metallicity has been derived by Reddy & Lambert (2019) and by the OCCASO project (Casamiquela et al. 2017, 2019; Carbajo-Hijarrubia et al. 2024). We have only one star in common for comparison.

**NGC 7086** - Located at a Galactocentric distance of approximately 8.6 kpc, this young OC ( $\approx 200$  Myr old, Cantat-Gaudin et al. 2020) has not yet been chemically characterized in the literature. The only reference we found is in Fu et al. (2022), based on the LAMOST low-resolution spectra.

**The “new” Gaia clusters** - UBC 3, UBC 60/COIN-Gaia 11, UBC 141, UBC 169, UBC 170, UBC 194, UBC 577, UBC

**Table 1.** Summary of the clusters analyzed in this work, including their properties and the number of stars in each cluster (N). Age,  $A_V$ , distance, and  $R_{GC}$  are from Cantat-Gaudin et al. (2020).

Cluster	Other names	N	Age (Gyr)	$A_V$ (mag)	Dist. (pc)	$R_{GC}$ (pc)	[Fe/H]	References
Alessi 1	Casado-Alessi 1	4	1.45	0.08	689	8726	1,2	
Alessi-Teutsch 11	ASCC 112, Alessi 46	1	0.14	0.37	634	8335	1	
Basel 11b	FSR 877	3	0.23	1.56	1793	10121	1,3	
COIN-Gaia 30	-	1	0.26	1.25	767	8804	1	
Collinder 350	-	2	0.59	0.52	371	8021	1,4	
Collinder 463	-	2	0.11	0.79	849	8874	1	
Gulliver 18	Collinder 416	1	0.04	1.59	1595	7816	1	
Gulliver 24	-	1	0.18	1.05	1498	9131	1	
Gulliver 51	-	1	0.36	1.42	1536	9410	4	
IC 4756	Collinder386, Melotte 210	12	1.29	0.29	506	7938	2,5,6,7,8,9	
NGC 2437	M 46, Melotte75	5	0.30	0.73	1511	9345	1,7	
NGC 2509	Melotte 81, Collinder 171	1	1.51	0.23	2495	9887	1	
NGC 2548	M 48, Melotte 85	3	0.40	0.15	772	8857	1,7,9,10,11	
NGC 2632	M 44, Praesepe	2	0.68	0.00	183	8479	2,3,5,9,10,12,13,14	
NGC 2682	M 67	2	4.27	0.07	889	8964	1,2,3,5,7,9	
NGC 6800	-	1	0.41	0.83	1012	7868	-	
NGC 6991	-	5	1.55	0.20	577	8333	9,15	
NGC 7044	Collinder 433	4	1.66	1.78	3252	8729	2,4,16	
NGC 7086	Collinder 437	2	0.19	1.81	1677	8632	17	
NGC 7209	Melotte 238, Collinder 444	2	0.43	0.53	1154	8525	1	
NGC 752	Melotte 12, Theia 1214	5	1.17	0.07	483	8669	3,5,9,18,19	
Ruprecht 171	-	7	2.75	0.68	1522	6895	4,9,16	
Stock 2	-	8	0.40	0.50	399	8619	15,20	
Tombaugh 5	-	3	0.19	2.07	1706	9768	1,21	
UBC 3	Alessi 161	1	0.13	0.98	1704	7223	9	
UBC 60	COIN-Gaia 11	1	0.79	1.25	669	8977	17	
UBC 131	Alessi 116, UPK 84	3	1.00	0.31	944	7980	2	
UBC 141	-	1	2.09	0.51	1315	8176	2,17	
UBC 169	-	2	0.30	0.26	1347	8749	17	
UBC 170	FoF 1800, LP 1800	3	0.33	1.25	1392	8809	-	
UBC 194	-	1	0.23	0.48	1361	9394	-	
UBC 577	Alessi 191	4	2.75	0.00	1122	7718	2	
UPK 219	-	1	0.15	1.20	873	8735	1	

**Notes.** References: (1) Zhang et al. (2021); (2) Viscasillas Vázquez et al. (2023); (3) Myers et al. (2022); (4) Casali et al. (2020a); (5) Netopil et al. (2016), High-quality spectroscopic metallicity, see original references there; (6) Bagdonas et al. (2018); (7) Ray et al. (2022); (8) Tsantaki et al. (2023); (9) Carbajo-Hijarrubia et al. (2024); (10) Spina et al. (2021); (11) Ramos et al. (2024); (12) D’Orazi et al. (2020); (13) Cummings et al. (2017); (14) Vejar et al. (2021); (15) Reddy & Lambert (2019); (16) Seshashayana et al. (2024); (17) Fu et al. (2022), LAMOST low-resolution spectra; (18) Lum & Boesgaard (2019); (19) Böcek Topcu et al. (2015); (20) Alonso-Santiago et al. (2021); (21) Baratella et al. (2018).

131/UPK 84, and UPK 219 (see Table 1 for alternative names) are new open clusters<sup>2</sup> discovered by Castro-Ginard et al. (2018, 2019, 2020) (the UBC clusters) and Sim et al. (2019) (the UPK clusters) using Gaia DR2 and DR3 data. For the UBC clusters, a clustering algorithm (DBSCAN) was used to detect overdensities in the astrometric space (position, parallax, and proper motions), followed by a neural network classifier to separate random clusterings from true clusters. For the UPK clusters, Sim et al. (2019) relied on a visual inspection of proper motion and spatial distributions. Most of these clusters were not yet studied spectroscopically, although UBC 60, UBC 131, UBC 141, and UBC 169 have metallicity based on LAMOST low-resolution spectra (Fu et al. 2022) or on intermediate-resolution Gaia-RVS spectra Viscasillas Vázquez et al. (2023). Only UBC 3 has been fully chemically characterized within the high-resolution project OCCASO (Carbajo-Hijarrubia et al. 2024).

### 3. Spectroscopic analysis

We first corrected the spectra for radial velocity (RV) and performed continuum normalization. For this purpose, we used the *iSpec* tool (Blanco-Cuaresma et al. 2014). The continuum normalization was carried out using a spline function with 60 splines of quadratic order. Table A.1 provides an overview of the properties of our giant stars in 14 open clusters. We refer to Casali et al. (2020a); Zhang et al. (2021, 2022); Alonso-Santiago et al. (2021) for the remainder of the sample. This table includes, for each star, Gaia DR3 (Gaia Collaboration et al. 2023b) right ascension and declination, magnitudes, and RV, along with the total exposure times, the resulting signal-to-noise ratio (S/N), and the estimated RV and associated error obtained from *iSpec*. There is a remarkable agreement between the RV measurements from Gaia DR3 and those from *iSpec*, with a mean difference of  $+0.08 \text{ km s}^{-1}$ . The comparison was done after the exclusion of a few binary stars, either already known or found by us based on RV differences (see Sect. 4 for more details).

<sup>2</sup> Actually, a few of the UBC and UPK clusters are rediscovery of objects already known, see the cited studies for the cross-matching with older catalogs.

**Table 2.** Stellar parameters obtained with LOTUS for the 95 stars presented in this work.

Star	Gaia DR3 ID	$T_{\text{eff}}$ (K)	$\log g$ (dex)	[Fe/H] (dex)	$\xi$ (kms $^{-1}$ )
Alessi 1 #2	402506369136008832	4986 $\pm$ 30	2.83 $\pm$ 0.07	-0.00 $\pm$ 0.01	1.30 $\pm$ 0.01
Alessi 1 #3	402505991180022528	4996 $\pm$ 30	2.84 $\pm$ 0.07	-0.01 $\pm$ 0.01	1.28 $\pm$ 0.01
Alessi 1 #5	402867593065772288	4939 $\pm$ 31	2.73 $\pm$ 0.08	-0.03 $\pm$ 0.01	1.35 $\pm$ 0.01
Alessi 1 #6	402880684126058880	4985 $\pm$ 32	2.87 $\pm$ 0.08	-0.01 $\pm$ 0.01	1.28 $\pm$ 0.01
Alessi Teutsch 11 #1	2184332753719499904	4517 $\pm$ 35	2.15 $\pm$ 0.11	-0.04 $\pm$ 0.01	1.76 $\pm$ 0.01
Basel 11b #1	3424056131485038592	4950 $\pm$ 35	2.51 $\pm$ 0.09	0.01 $\pm$ 0.01	1.81 $\pm$ 0.01
Basel 11b #2	3424055921028900736	5008 $\pm$ 33	2.64 $\pm$ 0.08	0.02 $\pm$ 0.01	1.77 $\pm$ 0.01
Basel 11b #3	3424057540234289408	4760 $\pm$ 34	2.55 $\pm$ 0.10	0.08 $\pm$ 0.01	1.47 $\pm$ 0.02
COIN-Gaia 30 #1	532533682228608384	4796 $\pm$ 35	2.41 $\pm$ 0.10	-0.04 $\pm$ 0.01	1.69 $\pm$ 0.01
Collinder 350 #1	4372743213795720704	4197 $\pm$ 53	1.65 $\pm$ 0.19	-0.15 $\pm$ 0.02	1.86 $\pm$ 0.02

**Notes.** Only an excerpt of the table is shown here. The full table is available at the CDS.

### 3.1. Stellar parameters

Spectroscopic parameters ( $T_{\text{eff}}$ ,  $\log g$ , metallicity [Fe/H]<sup>3</sup> and microturbulent velocity  $\xi$ ) were obtained using the equivalent width (EW) method. The line list for Fe I and II transitions used in this work is based on Li & Ezzeddine (2023). These authors combine iron lines from the Gaia-ESO line list (Jofré et al. 2014; Heiter et al. 2015, 2021) and from the R-Process Alliance (RPA) survey (Hansen et al. 2018; Sakari et al. 2018; Ezzeddine et al. 2020; Holmbeck et al. 2020). In total, we have 165 Fe I and 20 Fe II lines. The EWs were measured using the *smhr* tool<sup>4</sup> (Casey 2014). Our method involved measuring the EW for a single reference star (#5 from IC 4756) using *smhr*. Subsequently, we calculated the EWs for the rest of the sample using the reference star input masks with the *stellardiff* tool<sup>5</sup>. This code is specifically designed for differential analyses, allowing users to make assumptions about the local continuum around the spectral lines. This functionality helps minimize the effects of poor spectral normalization or unresolved features in the continuum. Additionally, we excluded any line with an EW greater than 200 mÅ and with an error exceeding 10 mÅ.

Initially, we employed the *qoyllur-quipu* (q2) LTE differential analysis code (Ramírez et al. 2014) on a test subsample of 14 open cluster stars, as routinely performed in previous works such as Casamiquela et al. (2017, 2019); Liu et al. (2016). The q2 tool is a Python package that enables users to use MOOG (Sneden 1973) to calculate atmospheric parameters and abundances based on the standard iron line excitation and ionization equilibrium techniques. The code works iteratively to adjust the parameters, aiming to minimize correlations with excitation potential ( $\chi$ ) and the reduced equivalent width (REW), while also reducing the differences between the mean iron abundances derived from Fe I and Fe II lines. A notable strength of this code is its capability to perform line-by-line differential analysis, which offers a more robust method for analyzing “twin” stars (as discussed in, for example, Meléndez et al. 2009). For the q2 method, we initially calculated differential parameters using the IC 4756 #5 as the reference for the entire sample. However, this approach proved inadequate due to the wide range of effective temperatures ( $T_{\text{eff}}$ ) and surface gravities ( $\log g$ ) exhibited by our cluster giants. To address this, we established criteria for selecting multiple reference stars, ensuring that the differences between each star and its chosen reference satisfied the conditions

<sup>3</sup> We adopt the standard spectroscopic notation of  $[\text{Fe}/\text{H}] = \log \frac{N(\text{Fe})_{\star}}{N(\text{H})_{\star}} - \log \frac{N(\text{Fe})_{\odot}}{N(\text{H})_{\odot}}$

<sup>4</sup> <https://github.com/andycasey/smhr>

<sup>5</sup> <https://github.com/andycasey/stellardiff>

of  $\Delta T_{\text{eff}} < 150$  K and  $\Delta \log g < 0.25$ . Ultimately, we identified four suitable reference stars (IC 4756 #4, #5, #13 and UBC 170 #1). To choose these reference stars, we first ran the q2 method to compute the absolute parameters for all the stars in the sample. We then used the absolute parameters of the reference stars to apply the q2 method again to derive the parameters for each subsample with their respective reference stars. However, recognizing the limitations of this method, which still resulted in a significant internal spread within each cluster, exceeding  $\approx 0.20$  dex (peak-to-valley) for giant stars, we opted to adopt an NLTE methodology and proceeded as follows.

We employed the code LOTUS (non-LTE Optimization Tool Utilized for the derivation of atmospheric Stellar parameters, Li & Ezzeddine 2023)<sup>6</sup>, which allows the derivation of atmospheric parameters ( $T_{\text{eff}}$ ,  $\log g$ , [Fe/H] and  $\xi$ ) based on EW measurements of Fe I and Fe II lines. LOTUS performs interpolations of a generalized curve of growth (GCOG) from a grid of theoretical EWs in both LTE and NLTE, following the methodology outlined by Boeche & Grebel (2016). Stellar parameters are derived by minimizing the slopes of excitation and ionization equilibrium through an iterative global minimization process, with uncertainties in the atmospheric parameters estimated using a Markov-Chain Monte Carlo algorithm, further details are provided by Li & Ezzeddine 2023 (see their Sect. 2.5). Figure B.1 show the corner plot from the posterior distribution of the stellar parameters and their uncertainty for IC 4756 #5. Users can select either LTE or NLTE modes. When considering cool giants, adopting the NLTE approach over LTE-based analyses is crucial for accurately modeling their atmospheres. These stars have low surface gravities and densities, which prevent them from maintaining collisional equilibrium in their outer layers, causing a departure from LTE. NLTE effects arise from these imbalances, particularly in the ionization balance of elements like iron, and can significantly impact the derived abundances and stellar parameters (see e.g., Bergemann et al. 2012; Lind et al. 2022, and references therein). Therefore, in this study, we chose to run LOTUS with NLTE corrections, using the following input parameters to represent the stars in our sample: stellar type K ( $T_{\text{eff}}$  ranging from 4000 K to 5200 K), giants ( $\log g$  between 0.5 dex and 3.0 dex), and metal-rich ([Fe/H] from  $-0.5$  to  $0.5$ ). We ran LOTUS on the 33 SPA open clusters, which comprises 95 giant stars. In Table 2, we report the derived stellar parameters  $T_{\text{eff}}$ ,  $\log g$ , [Fe/H], and  $\xi$  for a subset of the sample. The full table is available at CDS<sup>7</sup>. The uncertainties in [Fe/H] were calculated using  $\sigma / \sqrt{n}$ , where  $\sigma$  is the standard deviation of the Fe I lines

<sup>6</sup> <https://github.com/Li-Yangyang/LOTUS>

<sup>7</sup> <http://cdsweb.u-strasbg.fr/cgi-bin/qcat?J/A+A/>

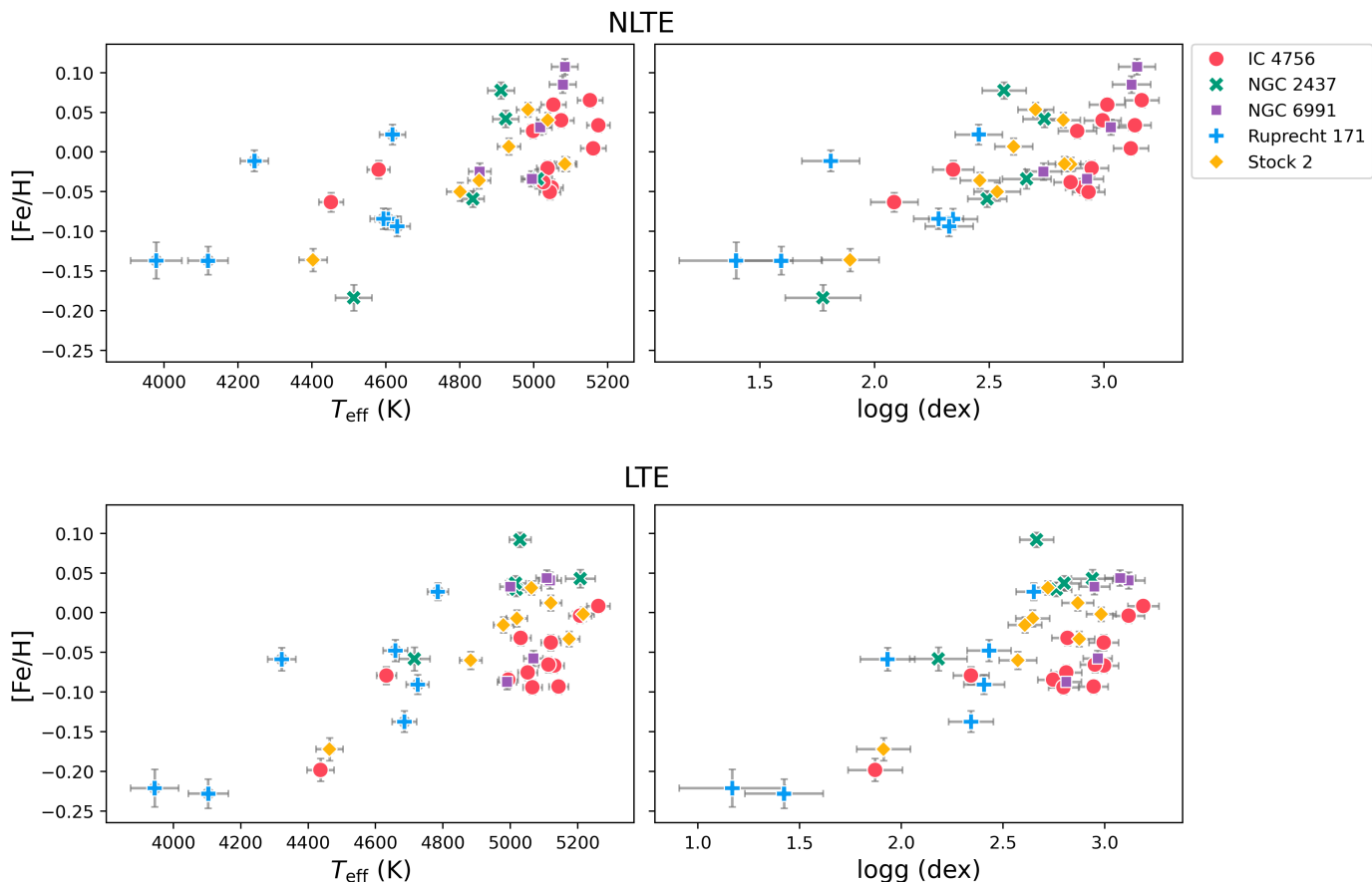


**Fig. 2.** Atmospheric parameters  $[Fe/H]$ ,  $T_{\text{eff}}$ , and  $\log g$  obtained with LOTUS for clusters containing more than five stars. The first row presents the NLTE results, while the second row shows the LTE results.

given by LOTUS, and  $n$  is the total number of Fe I lines used in the analysis.

Figure 2 presents the stellar parameters  $[Fe/H]$ ,  $T_{\text{eff}}$ , and  $\log g$  for clusters containing more than five giant stars. Looking at stars in the same cluster, a noticeable trend emerges between metallicity and effective temperature, with cooler stars (those with  $T_{\text{eff}} \approx 4600$  K) generally exhibiting lower metallicities. This trend is also present when considering surface gravity, which is to be expected as  $T_{\text{eff}}$  and gravity are correlated in the sample. Indeed, were the trend with  $T_{\text{eff}}$  be removed, the correlation with  $\log g$  would disappear as well. This pattern is not new and has been discussed in the literature (see, e.g., Casali et al. 2020a; Beeson et al. 2024).

Determining the underlying cause of these trends is complex and may be attributed to several factors, including continuum displacement in cooler giants, the influence of blended features, the selection of line lists and atomic parameters. Recently, Kos et al. (2025) reported abundance trends related to stellar parameters, particularly  $T_{\text{eff}}$ , for open clusters in GALAH DR4 (Buder et al. 2024). We refer to Kos et al. (2025) for a comprehensive discussion of the potential explanations for this trend. Additionally, as also emphasized in Kos et al. (2025), atomic diffusion cannot explain the observed trend, as it operates at different parameters and evolutionary stages, leading to trends that differ from those observed. Finally, a NLTE analysis reduces the discrepancies between warmer and cooler stars within the same clusters; however, it does not completely resolve the issue. This is clearly illustrated in Fig. 2, where we compare LTE (lower panel) and NLTE parameters obtained using LOTUS. Given the

amplitude trends calculated in Kos et al. (2025), our results are consistent with GALAH stars for most elements. However, we observe larger internal variation for Sr and Y, which is primarily driven by a single cluster, Ruprecht 171, where a few cold stars contribute to the discrepancy.

In cases with a large number of stars per cluster, one might consider detrending these results, as done in Kos et al. (2025). However, given the statistic limitation in our case, we have chosen to present our abundance measurements as they are, recognizing that this trend may introduce an internal precision limitation of less than  $\approx 0.1$  dex.

A direct, full comparison of LTE and NLTE results is not the focus of the present paper and we conclude the exercise by showing the differences between LTE and NLTE parameters in Fig. C.1. There, a clear positive trend is present, indicating that stars with larger (and positive) LTE–NLTE temperature differences also show larger differences in surface gravity. This suggests that LTE analysis tends to overestimate both  $T_{\text{eff}}$  and  $\log g$ , and that NLTE analysis mitigates these biases, yielding more consistent parameters across different stellar types.

### 3.2. Elemental abundances

To derive elemental abundances for species other than iron using NLTE grids in real-time (rather than through posterior corrections), only two spectral codes are currently available to our knowledge. These are the Python version of SME (Spectroscopy Made Easy, see Piskunov & Valenti 2017), pySME, developed by Wehrhahn et al. (2023), and the Python wrapper TSFitPy for

**Table 3.** NLTE chemical abundances derived with TSFitPy for the 95 stars presented in this work.

Star	[Mg/Fe]	[Si/Fe]	[Ti/Fe]	[Na/Fe]	[Al/Fe]	[Mn/Fe]	[Co/Fe]	[Ni/Fe]	[Sr/Fe]	[Y/Fe]	[Eu/Fe]
Alessi 1 #2	-0.036 ± 0.05	0.040 ± 0.05	0.047 ± 0.03	0.115 ± 0.01	-0.042 ± 0.01	0.027 ± 0.06	-0.058 ± 0.07	0.067 ± 0.06	0.014 ± 0.05	0.213 ± 0.03	-
Alessi 1 #3	-0.010 ± 0.05	0.012 ± 0.04	0.079 ± 0.03	0.123 ± 0.01	0.004 ± 0.01	0.008 ± 0.07	-0.064 ± 0.06	0.078 ± 0.06	-0.009 ± 0.05	0.172 ± 0.02	0.143 ± 0.05
Alessi 1 #5	-0.028 ± 0.05	-0.045 ± 0.02	0.044 ± 0.02	0.112 ± 0.01	-0.024 ± 0.05	0.015 ± 0.06	-0.066 ± 0.06	0.045 ± 0.05	0.044 ± 0.05	0.170 ± 0.03	-
Alessi 1 #6	-0.025 ± 0.05	0.015 ± 0.05	0.054 ± 0.03	0.079 ± 0.01	-0.045 ± 0.01	0.015 ± 0.06	-0.055 ± 0.06	0.092 ± 0.06	0.031 ± 0.05	0.184 ± 0.03	0.05 ± 0.05
Alessi Teutsch 11 #1	-0.097 ± 0.05	0.014 ± 0.02	0.024 ± 0.02	-0.065 ± 0.01	-0.047 ± 0.02	-0.086 ± 0.11	-0.077 ± 0.06	-0.121 ± 0.03	-0.041 ± 0.05	0.166 ± 0.05	-
Basel 11b #1	-0.095 ± 0.05	-0.091 ± 0.02	-0.025 ± 0.03	0.106 ± 0.01	0.003 ± 0.05	-0.098 ± 0.10	-0.126 ± 0.07	-0.057 ± 0.05	-0.025 ± 0.05	0.117 ± 0.05	0.153 ± 0.05
Basel 11b #2	-0.064 ± 0.05	-0.066 ± 0.05	0.028 ± 0.02	0.150 ± 0.05	-0.009 ± 0.05	-0.047 ± 0.06	-0.083 ± 0.06	0.020 ± 0.06	0.064 ± 0.05	0.239 ± 0.05	0.223 ± 0.05
Basel 11b #3	-0.075 ± 0.05	-0.085 ± 0.02	0.032 ± 0.02	-0.051 ± 0.02	-0.039 ± 0.05	-	-0.060 ± 0.06	-0.027 ± 0.05	0.287 ± 0.05	0.336 ± 0.06	0.121 ± 0.05
COIN-Gaia 30 #1	-0.067 ± 0.05	-0.093 ± 0.02	0.012 ± 0.03	0.093 ± 0.01	-0.047 ± 0.05	-0.115 ± 0.09	-0.098 ± 0.06	-0.080 ± 0.05	0.119 ± 0.05	0.205 ± 0.05	0.132 ± 0.05
Collinder 350 #1	-0.034 ± 0.05	0.019 ± 0.03	0.063 ± 0.03	0.146 ± 0.04	0.020 ± 0.03	-0.201 ± 0.13	-0.032 ± 0.06	-0.201 ± 0.13	0.303 ± 0.05	0.440 ± 0.05	-

**Notes.** Only an excerpt of the table is shown here. The full table is available at the CDS.

Turbospectrum version 20 (Plez 2012), as described in Gerber et al. (2023) and Storm & Bergemann (2023). Our chosen strategy was to adopt the latter option. TSFitPy allows the computation of synthetic spectra while incorporating NLTE corrections. The tool employs the Nelder-Mead algorithm to fit the normalized synthetic stellar spectra generated by Turbospectrum, minimizing the  $\chi^2$  value in the process. The code offers access to two grids of stellar model atmospheres: the 1D line-blanketed hydrostatic MARCS models (Gustafsson et al. 2008) and average 3D Stagger models (Magic et al. 2013a,b). In this study, we chose to use the 1D MARCS stellar grid.

We determined NLTE abundances for 11 chemical elements: Mg, Si, Ti, Na, Al, Mn, Co, Ni, Sr, Y, and Eu. In principle, a few more elements could have been included; however, the Ca lines were saturated, the Ba abundances appeared unrealistically high, preventing reliable measurements. The line list was constructed through a careful selection of isolated, unblended, and sufficiently strong lines within our spectral range. Most lines originate from the Gaia-ESO Survey linelist, with Sr I 4607 Å supplemented from VALD database<sup>8</sup>. For Eu, only the 6645 Å line was used, as the strong resonance line at 4129 Å is blended at the metallicity of our sample stars. We have included hyperfine splitting when needed (Mn, Co, and Eu lines). The complete line list is provided in Table D.1.

The abundances were calculated as the average of the values derived for each line and the associated uncertainties were computed using  $\sigma/\sqrt{n}$ , where  $\sigma$  is the standard deviation and  $n$  is the number of stars per cluster. For the cases when only one line was used, we adopted 0.05 dex as uncertainty, as it is the typical mean abundance uncertainty in our sample (see Table E.1 for sensitivities to stellar parameters). The chemical abundances for a subset of stars are presented in Table 3 (the full table is available at CDS<sup>9</sup>).

We established our abundance scale by analyzing a solar spectrum, using a spectrum of Ganymede obtained with the HARPS spectrograph on the 3.6 m ESO telescope. The stellar parameters adopted for the Sun are:  $T_{\text{eff}}=5771$  K,  $\log g=4.44$ ,  $\log(\text{Fe})=7.52$  and  $\xi=0.95$  km s<sup>-1</sup>. The absolute solar abundances referenced by TSFitPy are sourced from Magg et al. (2022). On the other hand, the determined solar abundances are as follows:  $A(\text{Mg}) = 7.47 \pm 0.10$ ,  $A(\text{Si}) = 7.49 \pm 0.04$ ,  $A(\text{Ti}) = 5.00 \pm 0.03$ ,  $A(\text{Na}) = 6.24 \pm 0.01$ ,  $A(\text{Al}) = 6.44 \pm 0.02$ ,  $A(\text{Mn}) = 5.48 \pm 0.02$ ,  $A(\text{Co}) = 4.84 \pm 0.07$ ,  $A(\text{Ni}) = 6.20 \pm 0.03$ ,  $A(\text{Sr}) = 2.72 \pm 0.10$ , and  $A(\text{Y}) = 1.98 \pm 0.04$ . Compared to the results of Asplund et al. (2009) and Magg et al. (2022), our solar abundances are consistent within  $2\sigma$  uncertainties, except for Y, which exhibits a deviation of  $4\sigma$ . The Eu II line at 6645 Å was too weak in the solar spectrum to yield a reliable

abundance measurement, and therefore no solar reference value could be determined. We adopted the value by Magg et al. (2022) of  $A(\text{Eu})_{\odot}=0.52$ . All other abundance ratios for our sample stars have been computed adopting the solar abundances derived in the present study.

We checked for correlations of  $[X/H]$  ratios with temperature and surface gravity considering the same open clusters in Fig. 2, and the results are shown in Fig. F.1. Within uncertainties, we find no significant trends for Mg, Si, Ti, Na, Al, as their behavior remains generally flat. However, for Mn, Co, Ni, Sr, Y and Eu, the abundances increase slightly with temperature (and  $\log g$ ) and there is also notable scatter. Moreover, for Sr and Y we have detected an upturn for  $T_{\text{eff}} \lesssim 4500$  K.

Table 4 shows the mean abundances for the 33 OCs. The abundance of each cluster is the average considering its members and the error is given by  $\sigma/\sqrt{n}$ . For clusters with only one star, the uncertainty is the standard deviation. Among our clusters, some interesting cases exist, such as the super-solar metallicity OCs NGC 2509 with  $[\text{Fe}/H]=0.212 \pm 0.01$  and UBC 60 with  $[\text{Fe}/H]=0.227 \pm 0.01$ . On the other hand, Gulliver 51 and NGC 7044 exhibit the lowest values of our sample, with  $[\text{Fe}/H] \sim -0.2$  dex.

Overall, we confirm that all the open clusters display a solar-scaled chemical composition concerning the  $\alpha$  elements, specifically Mg, Si, and Ti and the iron peak elements Mn, Co, and Ni. While Na abundances are generally consistent with solar values within the uncertainties, they display the well-known trend correlated with age. Neutron-capture element Sr and Eu show a solar-scaled abundance pattern, whereas Y is slightly super-solar. Regarding the potential enhancement of s-process elements, which may be associated with magnetic activity at younger ages, we direct readers to Spina et al. (2018), Baratella et al. (2021), Nordlander et al. (2024), and the references therein for further discussion.

#### 4. Comparison with the literature

We used the open clusters IC 4756, NGC 752, NGC 6991 and UBC 3, which have been previously studied in the literature, for comparison with our results. Furthermore, as explained before, we incorporate open clusters previously analyzed by Casali et al. (2020a), D’Orazi et al. (2020), Zhang et al. (2021, 2022), and Alonso-Santiago et al. (2021). Some clusters studied by these authors have also been investigated in the literature through other independent studies. Here, we present a comprehensive comparison of all available data, integrating results from both our study and previous works to ensure consistency and identify any discrepancies. In this process, we limited to high-resolution, optical spectroscopy. The comparison results are summarized in Table G.1 and Fig. G.1.

<sup>8</sup> <https://vald.astro.uu.se/>

<sup>9</sup> <http://cdsweb.u-strasbg.fr/cgi-bin/qcat?J/A+A/>

**Table 4.** Mean cluster abundance ratios.

OC	[Fe/H]	[Mg/Fe]	[Si/Fe]	[Ti/Fe]	[Na/Fe]	[Al/Fe]	[Mn/Fe]	[Co/Fe]	[Ni/Fe]	[Sr/Fe]	[Y/Fe]	[Eu/Fe]
Alessi 1	-0.012 ± 0.01	-0.025 ± 0.01	0.005 ± 0.02	0.056 ± 0.01	0.107 ± 0.01	-0.027 ± 0.01	0.016 ± 0.01	-0.061 ± 0.01	0.071 ± 0.01	0.020 ± 0.01	0.185 ± 0.01	0.098 ± 0.03
AlessiTeutsch 11	-0.040 ± 0.01	-0.097 ± 0.05	0.014 ± 0.02	0.024 ± 0.02	-0.066 ± 0.01	-0.048 ± 0.02	-0.086 ± 0.11	-0.077 ± 0.06	-0.122 ± 0.03	-0.042 ± 0.05	0.166 ± 0.05	-
Basel 11b	0.035 ± 0.02	-0.078 ± 0.01	-0.081 ± 0.01	0.012 ± 0.02	0.069 ± 0.05	-0.015 ± 0.01	-0.072 ± 0.02	-0.090 ± 0.02	-0.021 ± 0.02	0.109 ± 0.08	0.231 ± 0.05	0.166 ± 0.03
COIN-Gaia 30	-0.040 ± 0.01	-0.069 ± 0.05	-0.093 ± 0.02	0.012 ± 0.03	0.093 ± 0.01	-0.047 ± 0.05	-0.115 ± 0.09	-0.098 ± 0.07	-0.080 ± 0.05	0.119 ± 0.05	0.205 ± 0.05	0.132 ± 0.05
Collinder 350	-0.030 ± 0.08	-0.085 ± 0.04	-0.047 ± 0.05	-0.047 ± 0.08	0.088 ± 0.04	0.020 ± 0.03	-0.202 ± 0.13	-0.096 ± 0.04	-0.130 ± 0.03	0.138 ± 0.12	0.293 ± 0.10	0.204 ± 0.05
Collinder 463	-0.057 ± 0.01	-0.083 ± 0.01	-0.023 ± 0.01	-0.015 ± 0.01	0.128 ± 0.01	-0.034 ± 0.01	-0.104 ± 0.01	-0.102 ± 0.01	-0.103 ± 0.01	-0.055 ± 0.01	0.178 ± 0.02	-
Gulliver 18	-0.011 ± 0.02	-0.061 ± 0.05	-0.047 ± 0.03	0.061 ± 0.04	0.262 ± 0.06	-0.023 ± 0.05	-	-0.057 ± 0.07	-0.192 ± 0.05	0.388 ± 0.05	0.393 ± 0.05	0.134 ± 0.04
Gulliver 24	-0.136 ± 0.02	0.020 ± 0.05	-0.004 ± 0.03	0.115 ± 0.03	0.115 ± 0.01	-0.001 ± 0.01	-0.134 ± 0.13	-0.021 ± 0.08	-0.129 ± 0.04	0.219 ± 0.05	0.150 ± 0.12	0.168 ± 0.04
Gulliver 51	-0.170 ± 0.01	-0.031 ± 0.05	0.111 ± 0.07	0.042 ± 0.06	-0.015 ± 0.01	-0.011 ± 0.01	-0.061 ± 0.09	-0.083 ± 0.06	-0.055 ± 0.04	-0.088 ± 0.05	0.104 ± 0.01	0.112 ± 0.05
IC 4756	-0.001 ± 0.01	-0.031 ± 0.01	-0.018 ± 0.01	0.112 ± 0.01	0.090 ± 0.01	-0.049 ± 0.01	0.027 ± 0.01	-0.048 ± 0.01	0.046 ± 0.01	0.093 ± 0.01	0.254 ± 0.01	0.134 ± 0.01
NGC 2437	-0.031 ± 0.04	-0.103 ± 0.02	-0.042 ± 0.02	-0.037 ± 0.04	0.119 ± 0.02	-0.038 ± 0.01	-0.115 ± 0.08	-0.191 ± 0.06	-0.076 ± 0.06	-0.111 ± 0.11	0.121 ± 0.05	0.096 ± 0.02
NGC 2509	0.212 ± 0.01	0.020 ± 0.05	0.103 ± 0.05	0.163 ± 0.05	0.121 ± 0.07	-0.032 ± 0.02	-	0.107 ± 0.06	0.157 ± 0.07	-0.020 ± 0.10	0.282 ± 0.06	-
NGC 2548	0.045 ± 0.03	-0.085 ± 0.01	-0.012 ± 0.04	-0.030 ± 0.06	0.094 ± 0.04	-0.061 ± 0.03	0.042 ± 0.00	-0.154 ± 0.07	0.019 ± 0.02	-0.010 ± 0.03	0.191 ± 0.06	0.050 ± 0.05
NGC 2632	0.163 ± 0.03	-0.049 ± 0.00	0.033 ± 0.01	0.049 ± 0.02	0.243 ± 0.04	-0.055 ± 0.01	0.099 ± 0.01	-0.045 ± 0.01	0.088 ± 0.02	-0.116 ± 0.02	0.078 ± 0.03	0.039 ± 0.05
NGC 2682	0.041 ± 0.01	0.025 ± 0.01	0.025 ± 0.01	0.142 ± 0.01	0.056 ± 0.01	0.007 ± 0.01	0.046 ± 0.04	0.016 ± 0.01	0.093 ± 0.01	-0.088 ± 0.04	0.090 ± 0.01	0.036 ± 0.02
NGC 6800	0.108 ± 0.01	-0.091 ± 0.05	-0.073 ± 0.04	0.081 ± 0.03	0.172 ± 0.01	-0.029 ± 0.03	0.021 ± 0.09	-0.087 ± 0.07	0.047 ± 0.06	0.043 ± 0.10	0.303 ± 0.06	0.080 ± 0.05
NGC 6991	0.033 ± 0.03	-0.055 ± 0.01	0.001 ± 0.01	0.117 ± 0.01	0.028 ± 0.01	-0.055 ± 0.01	0.075 ± 0.01	-0.048 ± 0.01	0.055 ± 0.01	0.058 ± 0.02	0.244 ± 0.02	0.075 ± 0.05
NGC 7044	-0.178 ± 0.04	-0.086 ± 0.04	-0.208 ± 0.01	-0.062 ± 0.06	0.097 ± 0.10	0.025 ± 0.03	-	-0.152 ± 0.05	-0.245 ± 0.04	0.934 ± 0.06	0.252 ± 0.08	-
NGC 7086	-0.081 ± 0.02	-0.087 ± 0.01	-0.012 ± 0.02	-0.023 ± 0.01	0.094 ± 0.01	-0.014 ± 0.01	-0.110 ± 0.00	-0.095 ± 0.01	-0.141 ± 0.02	-0.060 ± 0.01	0.170 ± 0.01	0.154 ± 0.05
NGC 7209	-0.020 ± 0.05	-0.072 ± 0.02	-0.008 ± 0.04	0.023 ± 0.02	0.221 ± 0.03	0.005 ± 0.04	-0.081 ± 0.05	-0.053 ± 0.03	-0.076 ± 0.05	0.027 ± 0.06	0.207 ± 0.07	-
NGC 752	0.023 ± 0.06	-0.052 ± 0.02	0.011 ± 0.03	0.111 ± 0.02	0.004 ± 0.02	-0.068 ± 0.02	0.049 ± 0.02	-0.040 ± 0.02	0.047 ± 0.02	0.059 ± 0.03	0.216 ± 0.02	0.085 ± 0.01
Ruprecht 171	-0.075 ± 0.02	-0.006 ± 0.02	0.032 ± 0.04	0.047 ± 0.02	0.049 ± 0.02	0.021 ± 0.02	-0.067 ± 0.05	-0.030 ± 0.01	-0.026 ± 0.03	0.177 ± 0.15	0.142 ± 0.06	0.078 ± 0.02
Stock 2	-0.019 ± 0.02	-0.101 ± 0.02	-0.081 ± 0.03	0.001 ± 0.01	0.089 ± 0.01	-0.039 ± 0.01	-0.030 ± 0.01	-0.114 ± 0.02	-0.050 ± 0.03	0.027 ± 0.01	0.209 ± 0.02	0.104 ± 0.05
Tombaugh 5	0.016 ± 0.04	-0.004 ± 0.04	-0.047 ± 0.05	-0.039 ± 0.06	0.133 ± 0.06	0.002 ± 0.04	-	-0.042 ± 0.05	-0.088 ± 0.08	-	0.234 ± 0.03	0.170 ± 0.01
UBC 3	0.005 ± 0.01	-0.050 ± 0.05	-0.058 ± 0.02	0.038 ± 0.03	0.097 ± 0.01	0.052 ± 0.05	0.028 ± 0.01	-0.087 ± 0.06	-0.065 ± 0.05	-0.024 ± 0.05	0.205 ± 0.05	0.184 ± 0.05
UBC 60	0.227 ± 0.01	-0.066 ± 0.05	-0.037 ± 0.05	0.110 ± 0.04	0.154 ± 0.02	-0.037 ± 0.03	0.159 ± 0.09	-0.055 ± 0.08	0.056 ± 0.05	0.005 ± 0.05	0.266 ± 0.05	-
UBC 131	0.052 ± 0.02	-0.014 ± 0.01	-0.020 ± 0.01	0.121 ± 0.01	0.055 ± 0.01	-0.054 ± 0.01	-	-0.054 ± 0.01	0.130 ± 0.01	0.095 ± 0.02	0.269 ± 0.02	-
UBC 141	-0.023 ± 0.01	0.079 ± 0.05	-0.015 ± 0.03	0.165 ± 0.03	-0.021 ± 0.01	-0.047 ± 0.01	-0.010 ± 0.07	-0.014 ± 0.07	0.061 ± 0.06	0.037 ± 0.05	0.189 ± 0.04	-
UBC 169	0.053 ± 0.02	-0.216 ± 0.05	-0.244 ± 0.03	-0.084 ± 0.04	0.062 ± 0.03	-0.053 ± 0.04	-	-0.173 ± 0.09	-0.218 ± 0.02	-0.139 ± 0.05	0.103 ± 0.05	-
UBC 170	0.091 ± 0.01	-0.125 ± 0.03	-0.119 ± 0.03	-0.063 ± 0.04	0.144 ± 0.02	-0.071 ± 0.01	-0.109 ± 0.09	-0.222 ± 0.08	-0.127 ± 0.06	-0.097 ± 0.03	0.203 ± 0.03	-
UBC 194	0.055 ± 0.01	-	-	-	-	-0.148 ± 0.05	0.016 ± 0.01	-	-0.355 ± 0.07	-	-	-
UBC 577	-0.033 ± 0.02	-0.030 ± 0.01	0.020 ± 0.02	0.106 ± 0.01	0.074 ± 0.00	0.017 ± 0.03	0.175 ± 0.08	-0.054 ± 0.02	0.065 ± 0.01	0.069 ± 0.01	0.239 ± 0.01	-
UPK 219	0.070 ± 0.01	-0.124 ± 0.05	-0.125 ± 0.02	-0.032 ± 0.02	0.091 ± 0.02	-0.018 ± 0.03	-0.091 ± 0.09	-0.118 ± 0.06	-0.079 ± 0.05	-0.019 ± 0.05	0.170 ± 0.05	0.120 ± 0.05

For  $T_{\text{eff}}$  and  $\log g$ , we compared our results with the literature both on a cluster-by-cluster basis, by calculating the mean difference (this work minus literature) for each OC using stars in common, and on a star-by-star basis for individual objects. Considering the four OCs that are new in the SPA framework, we identified in the literature eight common stars in IC 4756 (#0, #2, #4, #5, #7, #12, #13, #14), three in NGC 752 (#3, #4, #5), one in NGC 6991 (#1) and one in UBC 3 (#1) (see Table G.1 and Fig. G.1 for the references).

In general, there is a good agreement in the results, considering the mean differences in  $T_{\text{eff}}$  and  $\log g$ , as shown in Table G.1 and Fig. G.1. For [Fe/H] and [Mg/Fe] our results show an overall agreement, while [Si/Fe] is generally lower in this work. [Ti/Fe], [Na/Fe] and [Al/Fe] display some variations, typically up to 0.2 dex, with aluminium reaching -0.29 dex in NGC 752. [Mn/Fe] is generally consistent, with a maximum difference of 0.3 dex in NGC 752. [Co/Fe] and [Ni/Fe] are in good agreement, with differences up to 0.15 dex. For [Sr/Fe], with fewer clusters available for comparison, the maximum difference is -0.26 dex in UBC 3, while [Y/Fe] shows differences of around 0.2 dex. Similarly, [Eu/Fe] is available for a limited number of clusters, with a maximum difference of 0.18 dex. Notably, Jacobson et al. (2007) shows considerable variations for [Si/Fe], [Na/Fe], and [Al/Fe] in IC 4756 compared to our results. Note that the works presented here may use different solar scales, which could explain some of the observed differences.

Considering the SPA OCs previously published, Casali et al. (2020a) presented the spectral analysis of 15 stars in four OCs: Collinder 350, Gulliver 51, NGC 7044, and Ruprecht 171. The authors derived stellar parameters using both EW analysis with the Fast Automatic MOOG Analysis (FAMA, Magrini et al. (2013)) and a spectral fitting technique with ROTFIT (Frasca et al. 2006, 2019). One of the stars in Gulliver 51 (#2), identified as a fast rotator, was excluded from our analysis. The  $T_{\text{eff}}$  and  $\log g$  show a good agreement, as indicated by their mean differences (see Table G.1). More recently, Carbajo-Hijarrubia et al. (2024) also investigated Ruprecht 171, revealing three stars in common with

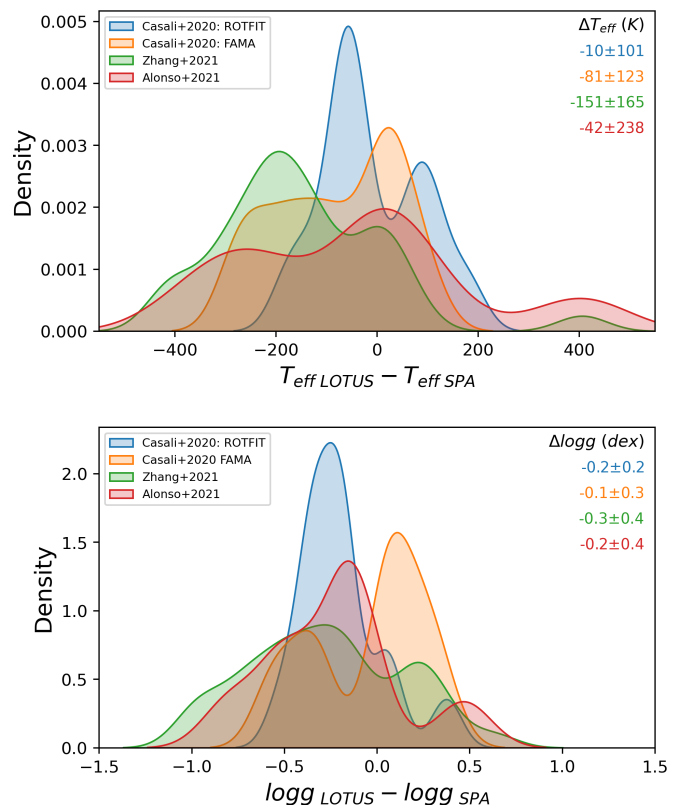


**Fig. 3.** Distribution of  $\Delta T_{\text{eff}}$  and  $\Delta \log g$  comparing LOTUS results to those from previous SPA studies. The histograms were smoothed. The colors indicate the different authors. Mean differences and standard deviations are displayed in each panel.

our study (#5, #6, and #8), which show general agreement, with a mean difference up to 220 K in temperature and 0.22 dex in [Fe/H].

Zhang et al. (2021) derived stellar parameters for 40 giant stars in 18 open clusters using EW measurements. From the initial set, we excluded six binary stars (Gulliver 37 #1, NGC 2437 #6, NGC 2548 #4, NGC 2682 #3 and #4, NGC 7082 #1 and #2) along with two stars (ASCC 11 #1 and NGC 2548 #4) that did not reach convergence with LOTUS. The results demonstrate good agreement in the mean differences of  $T_{\text{eff}}$  and  $\log g$ , with the exceptions of COIN-Gaia 30 and Gulliver 18. Furthermore, other authors have studied some of these OCs. We identified three stars in common in NGC 2548 (#1, #2, and #3), two stars in NGC 2682 (#1 and #2), and one star in Tombaugh 5 (#1), see Table G.1 for the references. All of them demonstrate overall consistency in  $T_{\text{eff}}$  and  $\log g$  with our results. Regarding the abundance measurements, Table G.1 indicates agreement for [Fe/H] and [Mg/Fe], while our results generally show lower [Si/Fe] values. Differences in [Ti/Fe] are observed, typically up to 0.2 dex, with a maximum of 0.28 dex for NGC 2682. Additionally, [Na/Fe], [Al/Fe], [Mn/Fe], [Co/Fe], and [Ni/Fe] exhibit agreement within 0.2 dex. Finally, [Y/Fe] values in our study are generally higher compared to the literature, reaching 0.26 for NGC 2548. We need however to consider that generally LTE results are reported.

Finally, Alonso-Santiago et al. (2021) analyzed 46 stars (both dwarfs and giants) in the open cluster Stock 2, determining the stellar atmospheric parameters using ROTFIT and abundances using SYNTHE and an optimization tool. In our analysis, we have 10 stars in common with Alonso-Santiago et al. (2021), although we excluded two binary stars (Stock 2 g3 and g5) from our sample. Additionally, as noted by Alonso-Santiago et al. (2021), Stock 2 was also studied by Reddy & Lambert (2019), with which we have two stars in common (#4 and #9). In general, the results are in fair agreement.

Figure 3 shows the smoothed distribution of the differences in  $T_{\text{eff}}$  and  $\log g$  for the stars in common considering this work and previous SPA studies. The distributions of  $\Delta T_{\text{eff}}$  and  $\Delta \log g$  reveal significant spreads, particularly for Zhang et al. (2021) and Alonso-Santiago et al. (2021), which appear broader compared to Casali et al. (2020a) (ROTFIT and FAMA). Notably, however, the majority of stars display differences concentrated around zero, indicating reasonable overall agreement between the results. The significant spreads in these distributions are primarily driven by a small subset of outlier stars. The mean values further suggest that LOTUS tends to yield lower values of  $T_{\text{eff}}$  and  $\log g$  compared to previous SPA results, as indicated by the leftward peaks in the distributions.

Figure 4 presents a comparative analysis of our results alongside previous SPA studies, focusing solely on SPA because it uses the same spectral data while employing different methodologies for calculating abundances. Notably, Zhang et al. (2022) applied NLTE corrections specifically to Na and Al, whereas Casali et al. (2020a) addressed NLTE effects for Fe but considered them negligible. Overall, we identify 19 SPA OCs in common for this comparison. Each line in the figure represents a distinct abundance, with our focus limited to [Fe/H],  $\alpha$ , and odd-Z elements. The comparison emphasizes several key points: i) The differences in [Fe/H] values are generally close to 0.0 dex, indicating strong consistency, except for the case of NGC 2509; ii) The [Mg/Fe] ratio displays more variation, with a few clusters deviating by approximately  $\pm 0.2$  dex; iii) [Si/Fe] results are slightly lower in the present analysis, particularly for Alessi Teutsch 11, Gulliver 18, Gulliver 24, and UPK 219; iv) Differences in [Ti/Fe] are present, with maximum value reaching around  $\pm 0.15$  dex; v) [Na/Fe] exhibits substantial discrepancy, approaching  $\pm 0.2$  dex; vi) [Al/Fe] shows similar trends to

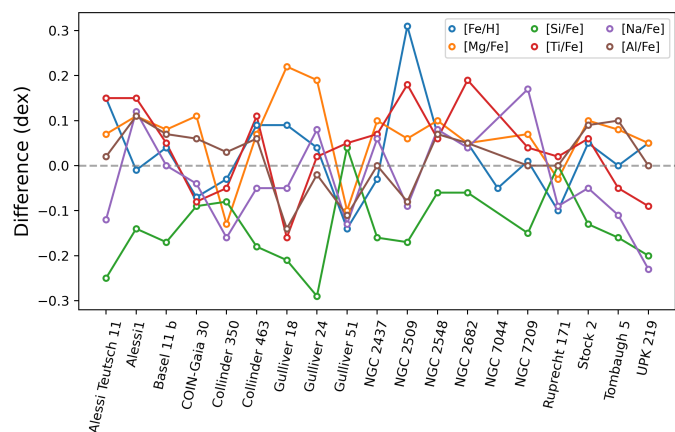


**Fig. 4.** Comparison between our abundance of Fe,  $\alpha$  and odd-z elements results and those from previous SPA studies for each open cluster. The lines represent different elements.

[Na/Fe], with variations present but generally less pronounced than those for Na. Overall, the comparison highlights that, despite some variations, the results presented here align well with previous studies for most elements. The observed differences in the comparison can primarily be attributed to three factors: the use of different line lists, variations in spectral analysis methodologies, and the adoption of NLTE abundances instead of LTE or a posteriori NLTE corrections. The methods used in this study resulted in reduced star-to-star scatter within each cluster, thereby providing higher internal precision.

## 5. Galactic trends

We derived abundances for Fe and 11 chemical elements that are synthesized in different nucleosynthesis sites, including Type II and Type Ia supernovae (SNe) and asymptotic giant branch stars (AGB), each contributing to the interstellar medium at different rates (see, e.g., Kobayashi et al. 2020; see also Romano et al. 2010, where uncertainties due to imperfect knowledge of stellar yields are discussed). More in general, studying how abundances change over time and across the Galactic disk is crucial for understanding the channels of element production and the various processes that have shaped the Milky Way's history (Molero et al. 2023). In this context, OCs present a favorable option, as they are distributed throughout the Galactic disk and encompass a wide range in ages that reflects a significant fraction of the lifespan of the thin disk. Furthermore, it is possible to characterize the chemistry of an OC using a small subset of its members.

We explored the abundance trends in the Galactic disk using the mean abundances for the 33 open clusters, combined with ages from Cantat-Gaudin et al. (2020). Our sample does not cover a large range in  $R_{\text{GC}}$ . Most of our clusters are within about 1 kpc from the Sun (see Table 1) and farther away from the Galactic center than the Sun, reflecting the fact that we observed from the Northern hemisphere. Conversely, our sample has broad coverage in age, from about 40 Myr to about 4 Gyr. We then opted to concentrate on the (possible) variations and evolution of abundances with age.

We included the OC sample from Spina et al. (2021) for visual comparison only, focusing specifically on the NLTE abundances reported in GALAH DR3 (Buder et al. 2021). Since our analysis is centered on NLTE abundances, we excluded comparisons with clusters from the Gaia-ESO survey (see, e.g., Magrini

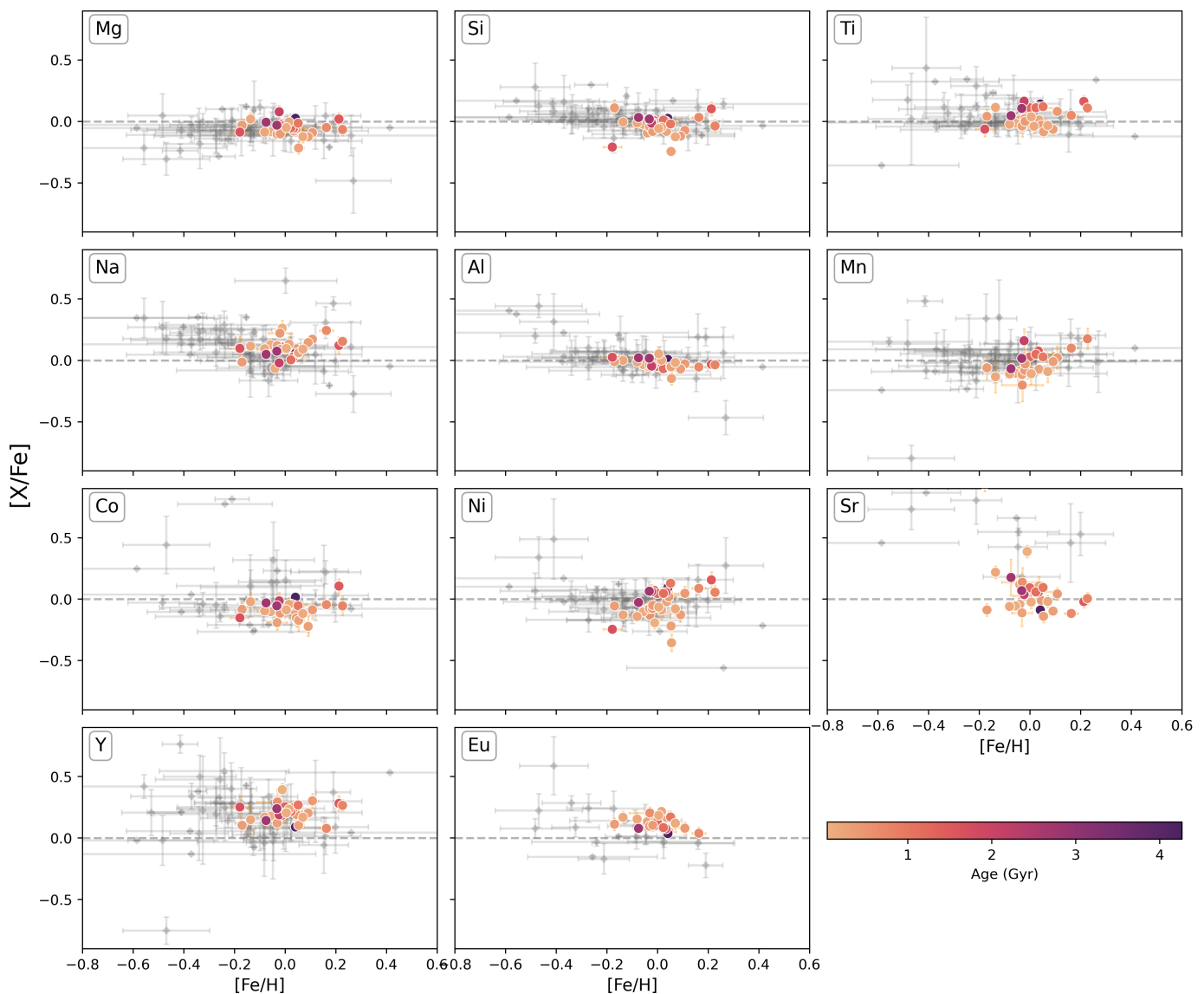


**Fig. 5.** Abundance  $[X/Fe]$  ratios as function of  $[Fe/H]$ . The gray diamonds represent the OCs compilation from GALAH (see Table H.1). Our results are color-coded according to the age.

et al. 2023). Instead, Mg and Na from APOGEE DR17 were compared, as these elements were derived using NLTE corrections. They were included using the sample from Myers et al. (2022). Although Spina et al. standardized data from APOGEE and GALAH, our calculations of mean abundances were based exclusively on GALAH. The ages presented in the GALAH and APOGEE OC compilation are taken from Cantat-Gaudin et al. (2020). Our discussion encompasses a total of 63 OCs from the original sample reported by Spina et al. (2021), which are listed in Table H.1, as well as an additional 84 OCs for Mg and 64 OCs for Na from Myers et al. (2022). The GALAH and the APOGEE OCs are represented by gray symbols in Figs. 5, 6, and 7.

The elements in the diagrams can be divided into categories:  $\alpha$  elements (Mg, Si, and Ti), iron-peak elements (Mn, Co, and Ni), odd- $Z$  elements (Na and Al), and neutron-capture elements (Sr, Y, and Eu). Overall, our findings are consistent with the distribution observed in GALAH, except for the  $[Sr/Fe]$  ratio; however, our abundance ratios show notably less scatter (see Fig. 5 and details in Sect. 5.4).

Regarding the age dependence, Fig. 6 illustrates the trend of  $[Fe/H]$  with age. As anticipated, there is no significant trend in OC metallicity relative to age, as the slope of the  $[Fe/H]$  versus age data is negligible. This supports the formation locus of a cluster as a more important factor for its chemical composition than the age—suggesting a lack of an age-metallicity relationship. Yet, it must be noted that only a mild evolution is expected in the last 4.5 Gyr in the solar neighborhood. It is important to mention that when focusing on very young ages, most (though not all) of the clusters show slightly subsolar iron abundances (Kos et al. 2021; Alonso-Santiago et al. 2024). This observation appears to challenge the conventional model of Galactic chemical evolution, unless there has been a recent inflow of metal-poor material (see, e.g., Spitoni et al. 2023; Palla et al. 2024). This situation is not typical, and we would anticipate different behavior based on modeling predictions. However, magnetic activity may indeed be influencing the results (Spina et al. 2020; Baratella et al. 2021).

For each of the  $[X/Fe]$  ratios we performed a linear fit of the abundance distributions versus age (shown in Fig. 7 as a

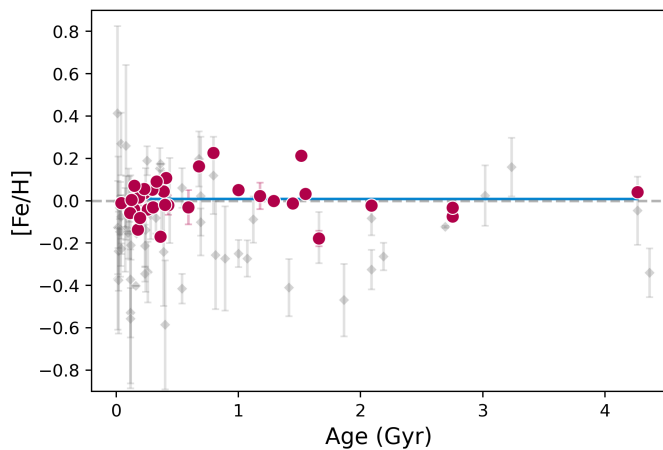


**Fig. 6.** Mean  $[\text{Fe}/\text{H}]$  per cluster as a function of age. The red points represent our sample of 33 open clusters, while the gray diamonds correspond to clusters from GALAH.

thick blue line). The corresponding slopes and their uncertainties are given in Table 5, alongside the values for the SPA sample from Zhang et al. (2022) (18 OCs) and the OCCASO and OCCAM projects (Carbajo-Hijarrubia et al. 2024; Myers et al. 2022), which include 26 and 84 OCs, respectively. Since Myers et al. (2022) did not provide slopes for  $[\text{X}/\text{Fe}]$  versus age, we derived them. The slopes obtained in this work are compatible within the errors with those used for comparison. For Ti, Mn, and Ni, our slopes ( $0.039 \pm 0.011$ ,  $0.040 \pm 0.016$ , and  $0.059 \pm 0.018$ , respectively) are steeper than those from other studies, which range from 0.002 to 0.012 for Ti, -0.008 to 0.003 for Mn, and 0.010 to 0.026 for Ni. In OCCAM, a positive slope is found for Na ( $0.004 \pm 0.009$ ), whereas this work ( $-0.021 \pm 0.012$ ), the previous SPA study, and OCCASO are in agreement with negative slopes. Yttrium has a shallower slope ( $-0.009 \pm 0.013$ ) in this work compared to OCCASO ( $-0.022 \pm 0.012$ ). No comparison is provided for Eu, as none of the references report a corresponding slope.

### 5.1. $\alpha$ elements

The  $\alpha$  elements are mainly produced by core-collapse supernovae (SNe), marking the final stage of the most massive stars ( $M \geq 10 M_{\odot}$ ). Since these massive stars have short lifetimes ( $\leq 10^{-2}$  Gyr), they quickly enrich the interstellar medium when compared with Fe, which is mainly produced on longer timescales via Type Ia SNe. In Fig. 5, Mg, Si and Ti shows a relatively flat behavior with increasing metallicity, consistent with observations from GALAH open clusters; Mg is also consistent with OCCAM open clusters. Figure 7 shows a decrease in the abundance ratios of Mg, Si, and Ti with younger ages. This trend mirrors observations made for nearby solar twins (Nissen 2015; Spina et al. 2016; Casali et al. 2020b) and field stars (see, e.g. Buder et al. 2019; Delgado Mena et al. 2019; Hayden et al. 2022). Such behavior is anticipated in the Galactic disk, which was initially formed from gas that was pre-enriched with  $\alpha$  elements, followed by additional enrichment from subsequent generations of stars. The observed decline in  $[\alpha/\text{Fe}]$  ratios with younger ages is consistent with predictions from Galactic chemical evolution models. In these models, successive generations of stars significantly contribute to  $\alpha$  element enrichment through core-collapse supernovae, while the delayed contributions from

**Table 5.**  $[\text{X}/\text{Fe}]$  versus age slopes and associated uncertainties.

Element	This work	SPA	OCCASO	OCCAM
Mg	$0.030 \pm 0.008$	$0.036 \pm 0.007$	$0.009 \pm 0.007$	$0.022 \pm 0.002$
Si	$0.023 \pm 0.013$	$-0.014 \pm 0.006$	$0.012 \pm 0.008$	$0.011 \pm 0.003$
Ti	$0.039 \pm 0.011$	$0.002 \pm 0.010$	$0.009 \pm 0.005$	$0.012 \pm 0.003$
Na	$-0.021 \pm 0.012$	$-0.031 \pm 0.040$	$-0.030 \pm 0.013$	$0.004 \pm 0.009$
Al	$0.009 \pm 0.006$	$0.009 \pm 0.008$	$0.020 \pm 0.011$	$0.026 \pm 0.004$
Mn	$0.040 \pm 0.016$	-	$0.003 \pm 0.007$	$-0.008 \pm 0.003$
Co	$0.030 \pm 0.010$	-	$0.007 \pm 0.005$	$0.016 \pm 0.008$
Ni	$0.059 \pm 0.018$	-	$0.026 \pm 0.006$	$0.010 \pm 0.002$
Sr	$0.025 \pm 0.036$	-	$-0.070 \pm 0.008$	-
Y	$-0.009 \pm 0.013$	-	$-0.022 \pm 0.012$	-
Eu	$-0.026 \pm 0.010$	-	-	-

**Notes.** The SPA slopes correspond to the sample of 18 open clusters presented in Zhang et al. (2022). For OCCASO, they correspond to 36 open clusters in the recent work of Carbajo-Hijarrubia et al. (2024). Values for  $[\text{X}/\text{Fe}]$  ratios and ages come from the original papers. For OCCAM, it is based on 84 high-quality open clusters from APOGEE DR17 Myers et al. (2022), except for Na (64), Al and Mn (82), and Co (61).

Type Ia supernovae dilute more and more efficiently the ejecta from core-collapse supernovae as the time goes by.

### 5.2. Odd-z elements

Sodium and aluminum are primarily generated by core-collapse supernovae, but they are also produced during the AGB phase (see Smiljanic et al. (2016)). In AGB models, Na production is notably affected by metallicity, exhibiting secondary behavior where stars with higher metallicities tend to have larger Na abundances. Figure 5 displays a generally flat trend for sodium in our sample, despite some scatter. While a distinct declining trend is observed in the GALAH open clusters, which demonstrate a wider range of metallicities compared to our sample, we must recognize the limitations posed by the smaller size of the SPA sample. This limitation introduces uncertainty regarding the interpretation of our findings, especially concerning the flatness and observed upward trend in  $[\text{Na}/\text{Fe}]$  for  $[\text{Fe}/\text{H}] > 0$ , which may be compatible with the GALAH distribution. This observation is consistent with recent findings by Owusu et al. (2024) and aligns with previous studies by e.g., Adibekyan et al. 2012; Nissen et al. 2020. In contrast to Na, the  $[\text{Al}/\text{Fe}]$  trends are more closely associated with those of the  $\alpha$  elements, likely due to their shared nucleosynthetic origins in massive stars (the AGB contribution to  $[\text{Al}/\text{Fe}]$  should be marginal in this metallicity range).

Figure 7 reveals several age-dependent trends, with Na decreasing and Al showing a mild increase as age progresses. The correlation between the behavior of Al and the  $\alpha$  elements over time has also been observed in solar twins (Casali et al. 2020b) and field stars (Delgado Mena et al. 2019). The observed trend of decreasing  $[\text{Na}/\text{Fe}]$  with age is consistent with what was found, for example, by Smiljanic et al. (2016, 2018). They observed an increase in the surface Na abundance for red giants belonging to OCs with turnoff mass larger than about  $2 M_{\odot}$  (i.e., younger than about 1 Gyr) and for Cepheids. This was attributed to evolutionary mixing processes; for these masses, additional Na is brought to the star surface at the first dredge-up, as confirmed by stellar evolutionary models predictions (see e.g., Lagarde et al. 2012; Ventura et al. 2013).

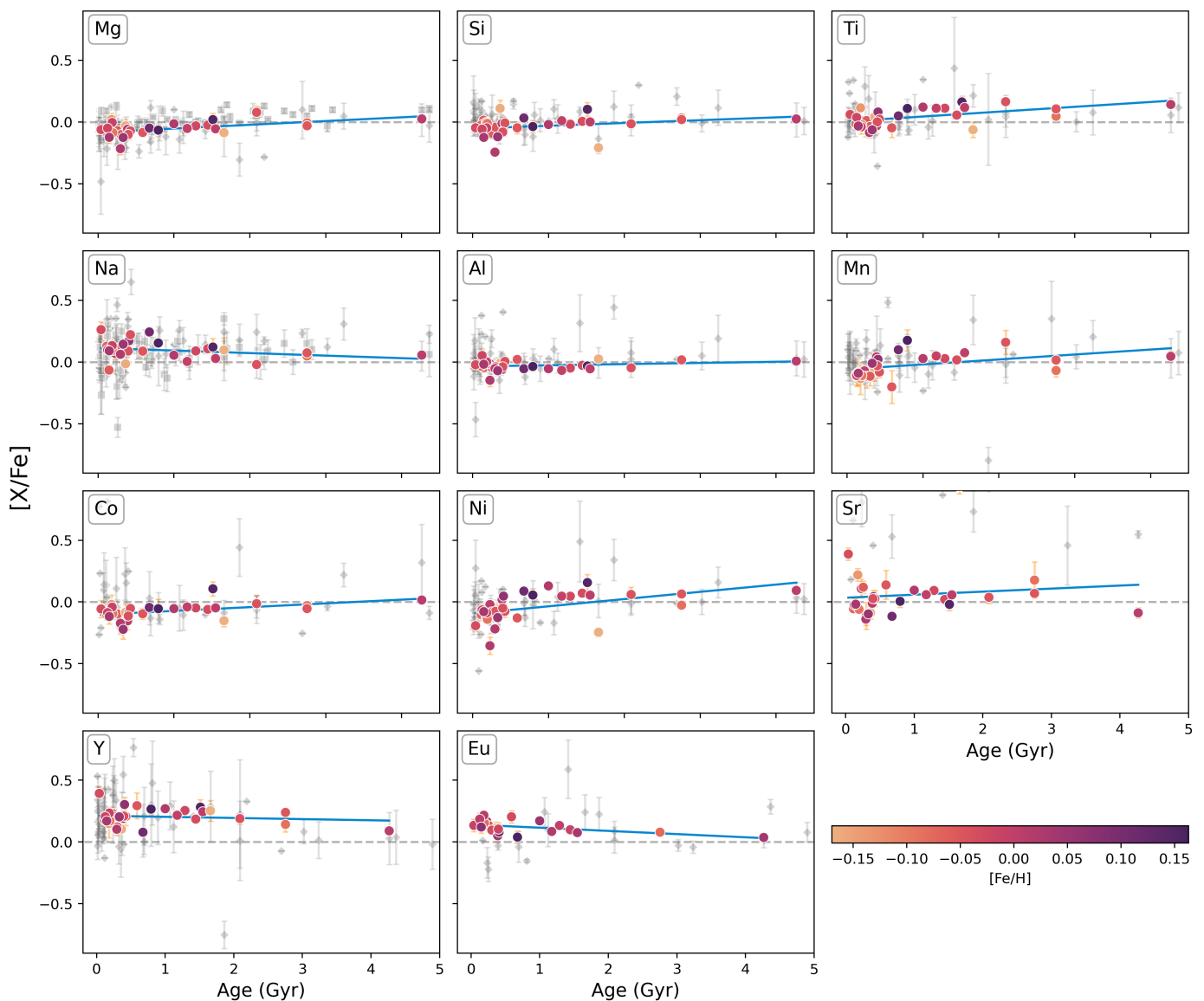


**Fig. 7.** Abundance  $[X/Fe]$  ratios as a function of age. The gray diamonds represent the OCs compilation from GALAH (see Table H.1) and the gray squares represent the OCs from OCCAM. Our results are color-coded according to  $[Fe/H]$ .

### 5.3. Iron-peak elements

Type Ia SNe, resulting from white dwarf stars in interacting binary systems (Whelan & Iben 1973; Iben & Tutukov 1984), are the primary source of iron-peak elements (Kobayashi et al. 2011, 2020; Nomoto & Leung 2018). Both core-collapse supernovae (CCSNe) and Type Ia supernovae contribute to the nucleosynthesis of iron-group elements, including manganese. For metallicities of  $[Fe/H] \lesssim -1$ , CCSNe dominate Mn production in the solar neighborhood. However, the transition point where Type Ia SNe begin to dominate varies across the Galactic disc: it occurs at lower  $[Fe/H]$  in the inner disc, where chemical evolution proceeds more rapidly, and at higher  $[Fe/H]$  in the outer disc, which evolves more slowly (Seitzzahl et al. 2013). Despite a general consensus on the qualitative roles of CCSNe and SNe Ia in producing Mn and Fe, the quantitative contributions remain uncertain. Consequently, the observed evolution of the  $[Mn/Fe]$  ratio with metallicity across the Galaxy is still not fully understood. Eitner et al. (2020) demonstrated that after accounting for NLTE corrections, the  $[Mn/Fe]$  ratio remains solar across all metallicities,

from approximately  $[Fe/H] \approx -4$  to 0. Our sample enables us to explore the chemical evolution of Mn at super-solar metallicities. As shown in Fig. 5, we observe an increasing trend in the  $[Mn/Fe]$  ratios with rising metallicity.

The  $[Co/Fe]$  ratios seem to follow a quite flat trend, in agreement with previous studies for thin disk stars (e.g., Reddy et al. 2003, 2006). On the other hand, we detected a mild decreasing trend of  $[Ni/Fe]$  for  $[Fe/H] < 0$ , although consistent with a solar-scaled pattern, within uncertainties (see e.g., Eitner et al. 2023); this is not seen in the GALAH sample.

Positive trends between Mn, Co and Ni and age are observed in Fig. 7. The production of Ni is primarily attributed to Type Ia supernovae, and a positive slope is not expected. This behavior is similar to the findings presented by Spina et al. (2021). The same trend is present in OCs studied by Carbajo-Hijarrubia et al. (2024), but not in the previous OCCASO studies. Recent 3D NLTE studies suggest that  $[Ni/Fe]$  may increase at lower metallicity due to NLTE effects (Storm et al. 2025), which could contribute to the trend in the metallicity regime covered by our sample. Manganese and Co display some mild increase with age,

consistent with the delayed contribution from Type Ia SNe and the metallicity dependence of their yields. As for Mn, it is important to highlight that Galactic chemical evolution models fail to align with the NLTE abundances reported by Eitner et al. (2020), unless one assumes a threefold increase in the Mn yields from core-collapse SNe. This is clearly illustrated in the work of Palla (2021) (see their Fig. 13), which also demonstrates that Mn can serve as an effective tool to differentiate between various SNIa yields, especially when precise measurements for metal-rich stars, such as those in this study, are available.

#### 5.4. Neutron-capture elements

Elements heavier than iron are primarily formed through neutron-capture processes, with only a few proton-rich nuclei formed by photodisintegration. Two primary neutron-capture mechanisms have been identified in nature: the slow (s) and rapid (r) processes. These processes occur at opposite ends of the neutron density range, with the s process occurring at lower densities and the r process at extremely high densities. They are characterized by neutron capture timescales that are slower or faster, respectively, than the beta-decay timescale of unstable nuclei. Together, these processes account for the majority of the abundances of elements heavier than iron in the Solar System (see the recent reviews by Cowan et al. 2021 and Lugaro et al. 2023). For the s-process, the elements are predominantly produced in AGB (via the  $^{13}\text{C}(\alpha, n)^{16}\text{O}$  neutron source) or massive stars (via the  $^{22}\text{Ne}(\alpha, n)^{25}\text{Mg}$ ). For the r-process, the main production channel is still under debate (compact mergers, special CC SNe; see, e.g., Cowan et al. 2021).

We inferred elemental abundances for the s-process elements yttrium and strontium, while barium lines were heavily saturated and susceptible to significant uncertainties. For this reason, we do not publish Ba abundances (see also discussion in Baratella et al. 2021; Nordlander et al. 2024). In our targets, along with the GALAH sample, most of the young clusters exhibit super-solar [Y/Fe] ratios. This observation, which has been previously noted in (young) open clusters (Magrini et al. 2018; Baratella et al. 2021), is not unexpected. However, whether this enhancement is genuine is strongly debated in the literature (D’Orazi et al. 2022). Although Sr and Y belong to the first peak of the s-process and share similar nucleosynthetic origins, they exhibit different behaviors in our analysis. In particular, Sr demonstrates a flatter distribution, with the majority of clusters showing abundances consistent with solar levels. In contrast, the GALAH open clusters show exceptionally high super-solar abundances, exceeding 0.5 dex. However, those values were inferred using the neutral Sr line at 6550 Å, known to be blended (see also the discussion in the GALAH DR3 paper, Buder et al. 2021). Such values are not consistent with any chemical evolution models. Therefore, we urge caution when interpreting these numbers, as they are subject to significant uncertainties. Europium abundances were also determined to trace the r-process contribution. Our findings indicate that these abundances are consistent with solar-scaled patterns, aligning with observations from the GALAH sample, although the GALAH data display a larger scatter. We find a slight positive slope with age, although not very significant. Delgado Mena et al. (2019) seem to indicate a trend in the opposite direction (see their Fig. 7). However, this is due to the inclusion of stars with ages larger than in our sample; when restricting to a maximum age of 4 Gyr, also their distribution is almost flat.

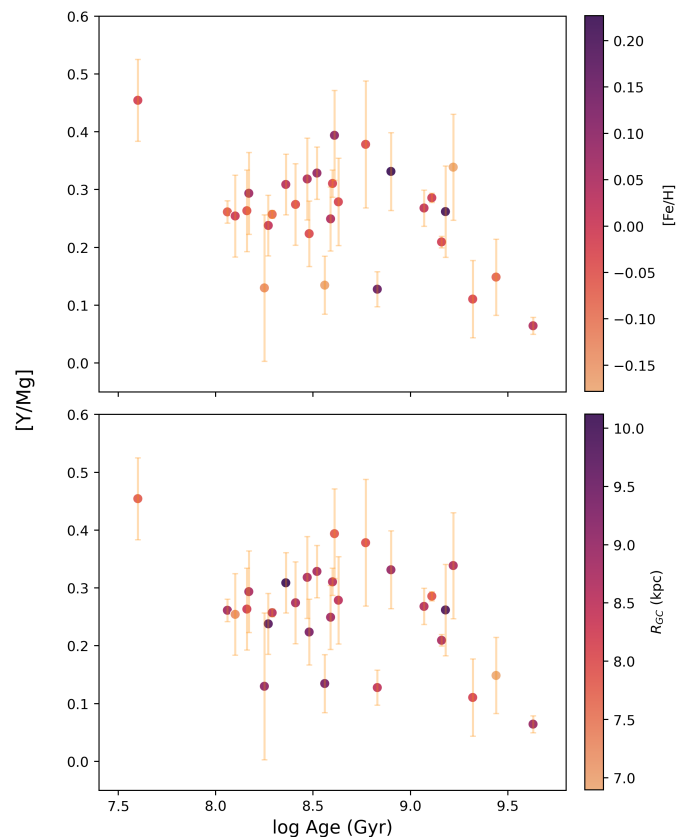


**Fig. 8.** [Y/Mg] as a function of age. The open clusters from this work are color-coded by [Fe/H] in the top panel and by  $R_{GC}$  in the bottom panel.

The interplay between the abundances of s-process elements and those of elements with opposite behaviors, such as the  $\alpha$  elements, enhances their correlation with stellar age. This relationship has been highlighted, for instance, by Nissen (2015); Spina et al. (2016, 2018); Delgado Mena et al. (2019), who identified the [Y/Mg] ratio (among others) as a reliable chronometer for Galactic evolution. However, the empirical relationships between n-capture elements and  $\alpha$  elements are not consistent across the Galactic disk. Recent studies (see, e.g., Feltzing et al. 2017; Casali et al. 2020b; Viscasillas Vázquez et al. 2022) have shown that these relationships vary depending on metallicity and the spatial location within the disk. This variation is significant, particularly given the presence of a metallicity gradient across the disk, especially in the inner part, up to 12–14 kpc (see, e.g., Donor et al. 2020). To accurately calibrate these empirical relations, samples with precise age determinations are essential, and open clusters represent one of the optimal choices within the high-metallicity regime (with [Fe/H] ranging from approximately -0.5 to 0.5 dex). Figure 8 presents the [Y/Mg] ratios plotted against the ages of the open clusters analyzed in this study. Our analysis reveals a nearly flat trend in [Y/Mg] versus age for clusters ranging from 100 Myr to approximately 1 Gyr, irrespective of the open clusters’ metallicities or their positions within the Galaxy (although we acknowledge that our data covers a limited range). The youngest cluster in our sample, Gulliver 18, with an age of about 40 Myr, displays the highest [Y/Mg] ratios, with [Y/Fe] ratios three times greater than the solar value. In contrast, M 67, the oldest cluster in our sample, exhibits the lowest [Y/Mg] ratio. Notably, the ratios for other clusters within this

range remain consistently flat with age, indicating that [Y/Mg] ratios may not be effective for dating the majority of OCs.

## 6. Summary

In this work, we examine 33 open clusters observed by the SPA project, comprising a total of 95 giant stars with high-resolution spectra from HARPS-N. We chemically characterized 13 open clusters within the SPA context and reanalyzed 20 previously studied clusters, creating a homogeneous and expanded sample within the SPA framework. We presented NLTE atmospheric parameters obtained using LOTUS through the equivalent width method and chemical abundances obtained via spectral synthesis with TSFitPy, covering ten elements from different nucleosynthesis groups.

We compared our results and those from the literature and found a good agreement. We explored the Galactic trends in abundance ratios [X/Fe] as a function of metallicity and age. For comparison, we used the open clusters studied by Spina et al. (2021), but with mean abundances derived using only GALAH DR3 original data and the open clusters by Myers et al. (2022) from the OCCAM survey. In general, our results follow similar trends to those observed in GALAH and APOGEE.

Regarding the age trends, the  $\alpha$  elements, such as Mg, Si, and Ti, show increasing trends with age. For the odd-Z elements, Na exhibits a decrease with age, while Al aligns more closely with the trends observed for  $\alpha$  elements. The iron-peak elements, Mn, Co, and Ni, display a positive correlation with age. Neutron-capture Y and Eu shows a decreasing trend with age. These trends are consistent with expectations from GCE models including the outcomes of nucleosynthesis processes in stars, except for Ni, and agree with previous studies.

In summary, this work added nine more open clusters with a full chemical characterization, and explored the age trends in elemental abundances, positive for Mg, Si, Ti, Al, Mn, Co and Ni and negative for Na and Y. These results illustrate the important role of open clusters as valuable tracers of Galactic chemical evolution, reinforcing that NLTE corrections are critical for accurate stellar parameter and abundance determination.

## Data availability

Tables 2 and 3 are only available in electronic form at the CDS via anonymous ftp to cdsarc.u-strasbg.fr (130.79.128.5) or via <http://cdsweb.u-strasbg.fr/cgi-bin/qcat?J/A+A/>.

*Acknowledgements.* This research used the facilities of the Italian Center for Astronomical Archive (IA2) operated by INAF at the Astronomical Observatory of Trieste. This work has made use of data from the European Space Agency (ESA) mission Gaia (<https://www.cosmos.esa.int/gaia>), processed by the Gaia Data Processing and Analysis Consortium (DPAC, <https://www.cosmos.esa.int/web/gaia/dpac/consortium>). Funding for the DPAC has been provided by national institutions, in particular the institutions participating in the Gaia Multilateral Agreement. This research has made use of the VizieR catalog access tool, CDS, Strasbourg, France (DOI : 10.26093/cds/vizier). The original description of the VizieR service was published in 2000, A&AS 143, 23. Use of the NASA's Astrophysical Data System and TOPCAT (Taylor 2005) are also acknowledged. We acknowledge funding from INAF MiniGrant 2022 (High resolution spectroscopy of open clusters) and the INAF grant Open Clusters and stellar structures in the local Galactic disk (ref. Antonella Vallenari) (CRA 1.05.23.05.19).

## References

Adibekyan, V. Z., Sousa, S. G., Santos, N. C., et al. 2012, A&A, 545, A32  
Alonso-Santiago, J., Frasca, A., Bragaglia, A., et al. 2024, A&A, 691, A317

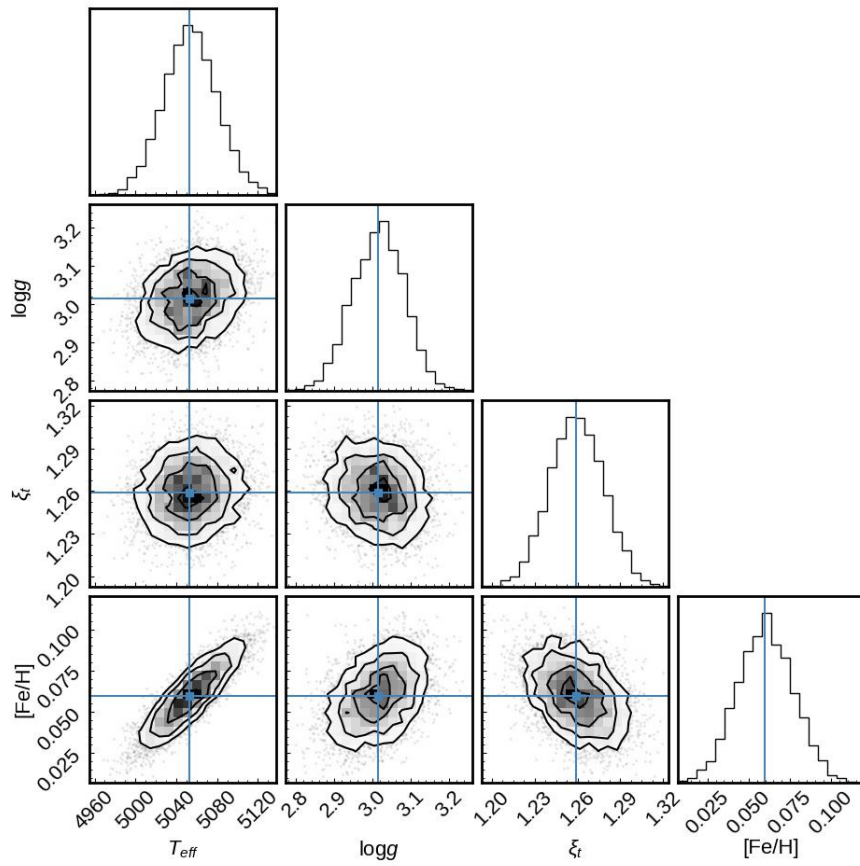
Alonso-Santiago, J., Frasca, A., Catanzaro, G., et al. 2021, A&A, 656, A149  
Asplund, M., Grevesse, N., Sauval, A. J., & Scott, P. 2009, ARA&A, 47, 481  
Bagdonas, V., Drazdauskas, A., Tautvaišienė, G., Smiljanic, R., & Chorniy, Y. 2018, A&A, 615, A165  
Baratella, M., Carraro, G., D'Orazi, V., & Semenko, E. A. 2018, AJ, 156, 244  
Baratella, M., D'Orazi, V., Sheminova, V., et al. 2021, A&A, 653, A67  
Beeson, K. L., Kos, J., de Grijs, R., et al. 2024, MNRAS, 529, 2483  
Bergemann, M., Lind, K., Collet, R., Magic, Z., & Asplund, M. 2012, MNRAS, 427, 27  
Bhattacharya, S., Agarwal, M., Rao, K. K., & Vaidya, K. 2021, MNRAS, 505, 1607  
Bijavara Seshashayana, S., Jönsson, H., D'Orazi, V., et al. 2024a, A&A, 683, A218  
Bijavara Seshashayana, S., Jönsson, H., D'Orazi, V., et al. 2024b, A&A, 689, A120  
Blanco-Cuaresma, S. & Fraix-Burnet, D. 2018, A&A, 618, A65  
Blanco-Cuaresma, S., Soubiran, C., Heiter, U., et al. 2015, A&A, 577, A47  
Blanco-Cuaresma, S., Soubiran, C., Heiter, U., & Jofré, P. 2014, A&A, 569, A111  
Böcek Topcu, G., Afşar, M., Schaeuble, M., & Sneden, C. 2015, MNRAS, 446, 3562  
Boeche, C. & Grebel, E. K. 2016, A&A, 587, A2  
Boesgaard, A. M., Lum, M. G., Chontos, A., & Deliyannis, C. P. 2022, ApJ, 927, 118  
Boffin, H. M. J., Jerabkova, T., Beccari, G., & Wang, L. 2022, MNRAS, 514, 3579  
Bossini, D., Vallenari, A., Bragaglia, A., et al. 2019, A&A, 623, A108  
Bragaglia, A. & Tosi, M. 2006, AJ, 131, 1544  
Buder, S., Kos, J., Wang, E. X., et al. 2024, arXiv e-prints, arXiv:2409.19858  
Buder, S., Lind, K., Ness, M. K., et al. 2019, A&A, 624, A19  
Buder, S., Sharma, S., Kos, J., et al. 2021, MNRAS, 506, 150  
Cantat-Gaudin, T., Anders, F., Castro-Ginard, A., et al. 2020, A&A, 640, A1  
Cantat-Gaudin, T., Vallenari, A., Sordo, R., et al. 2018, A&A, 615, A49  
Carbajo-Hijarrubia, J., Casamiquela, L., Carrera, R., et al. 2024, A&A, 687, A239  
Carraro, G., Monaco, L., & Villanova, S. 2014, A&A, 568, A86  
Carrera, R. & Pancino, E. 2011, A&A, 535, A30  
Casali, G., Magrini, L., Frasca, A., et al. 2020a, A&A, 643, A12  
Casali, G., Spina, L., Magrini, L., et al. 2020b, A&A, 639, A127  
Casamiquela, L., Blanco-Cuaresma, S., Carrera, R., et al. 2019, MNRAS, 490, 1821  
Casamiquela, L., Carrera, R., Blanco-Cuaresma, S., et al. 2017, MNRAS, 470, 4363  
Casey, A. R. 2014, PhD thesis, Australian National University, Canberra  
Castro-Ginard, A., Jordi, C., Luri, X., et al. 2020, A&A, 635, A45  
Castro-Ginard, A., Jordi, C., Luri, X., Cantat-Gaudin, T., & Balaguer-Núñez, L. 2019, A&A, 627, A35  
Castro-Ginard, A., Jordi, C., Luri, X., et al. 2018, A&A, 618, A59  
Cosentino, R., Lovis, C., Pepe, F., et al. 2012, in Society of Photo-Optical Instrumentation Engineers (SPIE) Conference Series, Vol. 8446, Ground-based and Airborne Instrumentation for Astronomy IV, ed. I. S. McLean, S. K. Ramsay, & H. Takami, 84461V  
Cowan, J. J., Sneden, C., Lawler, J. E., et al. 2021, Reviews of Modern Physics, 93, 015002  
Cummings, J. D., Deliyannis, C. P., Maderak, R. M., & Steinhauer, A. 2017, AJ, 153, 128  
Dalton, G., Trager, S., Abrams, D. C., et al. 2018, in Society of Photo-Optical Instrumentation Engineers (SPIE) Conference Series, Vol. 10702, Ground-based and Airborne Instrumentation for Astronomy VII, ed. C. J. Evans, L. Simard, & H. Takami, 107021B  
de Jong, R. S., Agertz, O., Berbel, A. A., et al. 2019, The Messenger, 175, 3  
De Silva, G. M., Freeman, K. C., Bland-Hawthorn, J., et al. 2015, MNRAS, 449, 2604  
Delgado Mena, E., Moya, A., Adibekyan, V., et al. 2019, A&A, 624, A78  
Donor, J., Frinchaboy, P. M., Cunha, K., et al. 2020, AJ, 159, 199  
D'Orazi, V., Baratella, M., Lugaro, M., Magrini, L., & Pignatari, M. 2022, Universe, 8, 110  
D'Orazi, V., Oliva, E., Bragaglia, A., et al. 2020, A&A, 633, A38  
Eitner, P., Bergemann, M., Hansen, C. J., et al. 2020, A&A, 635, A38  
Eitner, P., Bergemann, M., Ruitter, A. J., et al. 2023, A&A, 677, A151  
Ezzeddine, R., Rasmussen, K., Frebel, A., et al. 2020, ApJ, 898, 150  
Fanelli, C., Origlia, L., Oliva, E., et al. 2022, A&A, 660, A7  
Feltzing, S., Howes, L. M., McMillan, P. J., & Stokutė, E. 2017, MNRAS, 465, L109  
Frasca, A., Alonso-Santiago, J., Catanzaro, G., et al. 2019, A&A, 632, A16  
Frasca, A., Guillout, P., Marilli, E., et al. 2006, A&A, 454, 301  
Friel, E. D., Jacobson, H. R., & Pilachowski, C. A. 2010, AJ, 139, 1942  
Frinchaboy, P. M., Thompson, B., Jackson, K. M., et al. 2013, ApJ, 777, L1  
Fu, X., Bragaglia, A., Liu, C., et al. 2022, A&A, 668, A4  
Gaia Collaboration, Prusti, T., de Bruijne, J. H. J., et al. 2016, A&A, 595, A1

- Gaia Collaboration, Recio-Blanco, A., Kordopatis, G., et al. 2023a, *A&A*, 674, A38
- Gaia Collaboration, Vallenari, A., Brown, A. G. A., et al. 2023b, *A&A*, 674, A1
- Gao, X., Lind, K., Amarsi, A. M., et al. 2018, *MNRAS*, 481, 2666
- Gerber, J. M., Magg, E., Plez, B., et al. 2023, *A&A*, 669, A43
- Gilmore, G., Randich, S., Asplund, M., et al. 2012, *The Messenger*, 147, 25
- Gustafsson, B., Edvardsson, B., Eriksson, K., et al. 2008, *A&A*, 486, 951
- Hansen, T. T., Holmbeck, E. M., Beers, T. C., et al. 2018, *ApJ*, 858, 92
- Hao, C. J., Xu, Y., Wu, Z. Y., et al. 2022, *A&A*, 660, A4
- Hayden, M. R., Sharma, S., Bland-Hawthorn, J., et al. 2022, *MNRAS*, 517, 5325
- Heiter, U., Jofré, P., Gustafsson, B., et al. 2015, *A&A*, 582, A49
- Heiter, U., Lind, K., Bergemann, M., et al. 2021, *A&A*, 645, A106
- Holmbeck, E. M., Hansen, T. T., Beers, T. C., et al. 2020, *ApJS*, 249, 30
- Hunt, E. L. & Reffert, S. 2023, *A&A*, 673, A114
- Iben, Jr., I. & Tutukov, A. V. 1984, *ApJS*, 54, 335
- Jacobson, H. R., Friel, E. D., & Pilachowski, C. A. 2007, *AJ*, 134, 1216
- Jacobson, H. R., Pilachowski, C. A., & Friel, E. D. 2011, *AJ*, 142, 59
- Janes, K. A. 1979, *ApJS*, 39, 135
- Jian, M., Fu, X., Matsunaga, N., et al. 2024, *A&A*, 687, A189
- Jin, S., Trager, S. C., Dalton, G. B., et al. 2024, *MNRAS*, 530, 2688
- Jofré, P., Heiter, U., Soubiran, C., et al. 2014, *A&A*, 564, A133
- Kobayashi, C., Karakas, A. I., & Lugaro, M. 2020, *ApJ*, 900, 179
- Kobayashi, C., Karakas, A. I., & Umeda, H. 2011, *MNRAS*, 414, 3231
- Kos, J. 2024, *A&A*, 691, A28
- Kos, J., Bland-Hawthorn, J., Buder, S., et al. 2021, *MNRAS*, 506, 4232
- Kos, J., Buder, S., Beeson, K. L., et al. 2025, arXiv e-prints, arXiv:2501.06140
- Kounkel, M. & Covey, K. 2019, *AJ*, 158, 122
- Lagarde, N., Decressin, T., Charbonnel, C., et al. 2012, *A&A*, 543, A108
- Li, Y. & Ezzeddine, R. 2023, *AJ*, 165, 145
- Lind, K., Nordlander, T., Wehrhahn, A., et al. 2022, *A&A*, 665, A33
- Liu, F., Asplund, M., Yong, D., et al. 2016, *MNRAS*, 463, 696
- Liu, L. & Pang, X. 2019, *ApJS*, 245, 32
- Lucatello, S., Bragaglia, A., Vallenari, A., et al. 2023, *The Messenger*, 190, 13
- Lugaro, M., Pignatari, M., Reifarth, R., & Wiescher, M. 2023, *Annual Review of Nuclear and Particle Science*, 73, 315
- Lum, M. G. & Boesgaard, A. M. 2019, *ApJ*, 878, 99
- Magg, E., Bergemann, M., Serenelli, A., et al. 2022, *A&A*, 661, A140
- Magic, Z., Collet, R., Asplund, M., et al. 2013a, *A&A*, 557, A26
- Magic, Z., Collet, R., Hayek, W., & Asplund, M. 2013b, *A&A*, 560, A8
- Magrini, L., Randich, S., Friel, E., et al. 2013, *A&A*, 558, A38
- Magrini, L., Sestito, P., Randich, S., & Galli, D. 2009, *A&A*, 494, 95
- Magrini, L., Spina, L., Randich, S., et al. 2018, *A&A*, 617, A106
- Magrini, L., Viscasillas Vázquez, C., Spina, L., et al. 2023, *A&A*, 669, A119
- Majewski, S. R., Schiavon, R. P., Frinchaboy, P. M., et al. 2017, *AJ*, 154, 94
- Meléndez, J., Asplund, M., Gustafsson, B., & Yong, D. 2009, *ApJ*, 704, L66
- Molero, M., Magrini, L., Matteucci, F., et al. 2023, *MNRAS*, 523, 2974
- Monteiro, H. & Dias, W. S. 2019, *MNRAS*, 487, 2385
- Myers, N., Donor, J., Spoo, T., et al. 2022, *AJ*, 164, 85
- Netopil, M., Paunzen, E., Heiter, U., & Soubiran, C. 2016, *A&A*, 585, A150
- Nissen, P. E. 2015, *A&A*, 579, A52
- Nissen, P. E., Christensen-Dalsgaard, J., Mosumgaard, J. R., et al. 2020, *A&A*, 640, A81
- Nomoto, K. & Leung, S.-C. 2018, *Space Sci. Rev.*, 214, 67
- Nordlander, T., Baratella, M., Spina, L., & D'Orazi, V. 2024, *MNRAS*, 535, 2863
- Owusu, E. K., Buder, S., Ruitter, A. J., Seitzzahl, I. R., & Rodríguez-Segovia, N. 2024, *PASA*, 41, e092
- Pace, G., Danziger, J., Carraro, G., et al. 2010, *A&A*, 515, A28
- Pakhomov, Y. V., Antipova, L. I., Boyarchuk, A. A., et al. 2009, *Astronomy Reports*, 53, 660
- Palla, M. 2021, *MNRAS*, 503, 3216
- Palla, M., Magrini, L., Spitoni, E., et al. 2024, *A&A*, 690, A334
- Pancino, E., Carrera, R., Rossetti, E., & Gallart, C. 2010, *A&A*, 511, A56
- Piskunov, N. & Valenti, J. A. 2017, *A&A*, 597, A16
- Plez, B. 2012, *Turbospectrum: Code for spectral synthesis*, *Astrophysics Source Code Library*, record ascl:1205.004
- Ramírez, I., Meléndez, J., Bean, J., et al. 2014, *A&A*, 572, A48
- Ramos, A. A., Holanda, N., Drake, N. A., et al. 2024, *MNRAS*, 527, 6211
- Randich, S., Gilmore, G., & Gaia-ESO Consortium. 2013, *The Messenger*, 154, 47
- Randich, S., Gilmore, G., Magrini, L., et al. 2022, *A&A*, 666, A121
- Ray, A. E., Frinchaboy, P. M., Donor, J., Chojnowski, S. D., & Melendez, M. 2022, *AJ*, 163, 195
- Reddy, A. B. S., Giridhar, S., & Lambert, D. L. 2012, *MNRAS*, 419, 1350
- Reddy, A. B. S. & Lambert, D. L. 2019, *MNRAS*, 485, 3623
- Reddy, B. E., Lambert, D. L., & Allende Prieto, C. 2006, *MNRAS*, 367, 1329
- Reddy, B. E., Tomkin, J., Lambert, D. L., & Allende Prieto, C. 2003, *MNRAS*, 340, 304
- Romano, D., Karakas, A. I., Tosi, M., & Matteucci, F. 2010, *A&A*, 522, A32
- Sakari, C. M., Placco, V. M., Farrell, E. M., et al. 2018, *ApJ*, 868, 110
- Santos, N. C., Lovis, C., Pace, G., Melendez, J., & Naef, D. 2009, *A&A*, 493, 309
- Seitzzahl, I. R., Cescutti, G., Röpkke, F. K., Ruitter, A. J., & Pakmor, R. 2013, *A&A*, 559, L5
- Seshashayana, S. B., Jönsson, H., D'Orazi, V., et al. 2024, *A&A*, 683, A218
- Sestito, P., Bragaglia, A., Randich, S., et al. 2008, *A&A*, 488, 943
- Sestito, P., Randich, S., & Pallavicini, R. 2004, *A&A*, 426, 809
- Sim, G., Lee, S. H., Ann, H. B., & Kim, S. 2019, *Journal of Korean Astronomical Society*, 52, 145
- Smiljanic, R., Donati, P., Bragaglia, A., Lemasle, B., & Romano, D. 2018, *A&A*, 616, A112
- Smiljanic, R., Gauderon, R., North, P., et al. 2009, *A&A*, 502, 267
- Smiljanic, R., Romano, D., Bragaglia, A., et al. 2016, *A&A*, 589, A115
- Snedden, C. A. 1973, PhD thesis, University of Texas, Austin
- Spina, L., Meléndez, J., Karakas, A. I., et al. 2018, *MNRAS*, 474, 2580
- Spina, L., Meléndez, J., Karakas, A. I., et al. 2016, *A&A*, 593, A125
- Spina, L., Nordlander, T., Casey, A. R., et al. 2020, *ApJ*, 895, 52
- Spina, L., Ting, Y. S., De Silva, G. M., et al. 2021, *MNRAS*, 503, 3279
- Spitoni, E., Recio-Blanco, A., de Laverny, P., et al. 2023, *A&A*, 670, A109
- Storm, N. & Bergemann, M. 2023, *MNRAS*, 525, 3718
- Storm, N., Bergemann, M., Eitner, P., et al. 2025, *MNRAS*, 538, 3284
- Sun, Q., Deliyannis, C. P., Steinhauer, A., Twarog, B. A., & Anthony-Twarog, B. J. 2020, *AJ*, 159, 220
- Tautvaišienė, G., Edvardsson, B., Tuominen, I., & Ilyin, I. 2000, *A&A*, 360, 499
- Taylor, M. B. 2005, in *Astronomical Society of the Pacific Conference Series*, Vol. 347, *Astronomical Data Analysis Software and Systems XIV*, ed. P. Shopbell, M. Britton, & R. Ebert, 29
- Ting, Y.-S., De Silva, G. M., Freeman, K. C., & Parker, S. J. 2012, *MNRAS*, 427, 882
- Tsantaki, M., Delgado-Mena, E., Bossini, D., et al. 2023, *A&A*, 674, A157
- Vejar, G., Schuler, S. C., & Stassun, K. G. 2021, *ApJ*, 919, 100
- Ventura, P., Di Criscienzo, M., Carini, R., & D'Antona, F. 2013, *MNRAS*, 431, 3642
- Vermekar, N., Lucatello, S., Bragaglia, A., et al. 2024, *A&A*, 684, A85
- Viscasillas Vázquez, C., Magrini, L., Casali, G., et al. 2022, *A&A*, 660, A135
- Viscasillas Vázquez, C., Magrini, L., Spina, L., et al. 2023, *A&A*, 679, A122
- Wehrhahn, A., Piskunov, N., & Ryabchikova, T. 2023, *A&A*, 671, A171
- Whelan, J. & Iben, Jr., I. 1973, *ApJ*, 186, 1007
- Yong, D., Carney, B. W., Teixeira de Almeida, M. L., & Pohl, B. L. 2006, *AJ*, 131, 2256
- Zhang, R., Lucatello, S., Bragaglia, A., et al. 2022, *A&A*, 667, A103
- Zhang, R., Lucatello, S., Bragaglia, A., et al. 2021, *A&A*, 654, A77
- Zhao, G., Zhao, Y.-H., Chu, Y.-Q., Jing, Y.-P., & Deng, L.-C. 2012, *Research in Astronomy and Astrophysics*, 12, 723

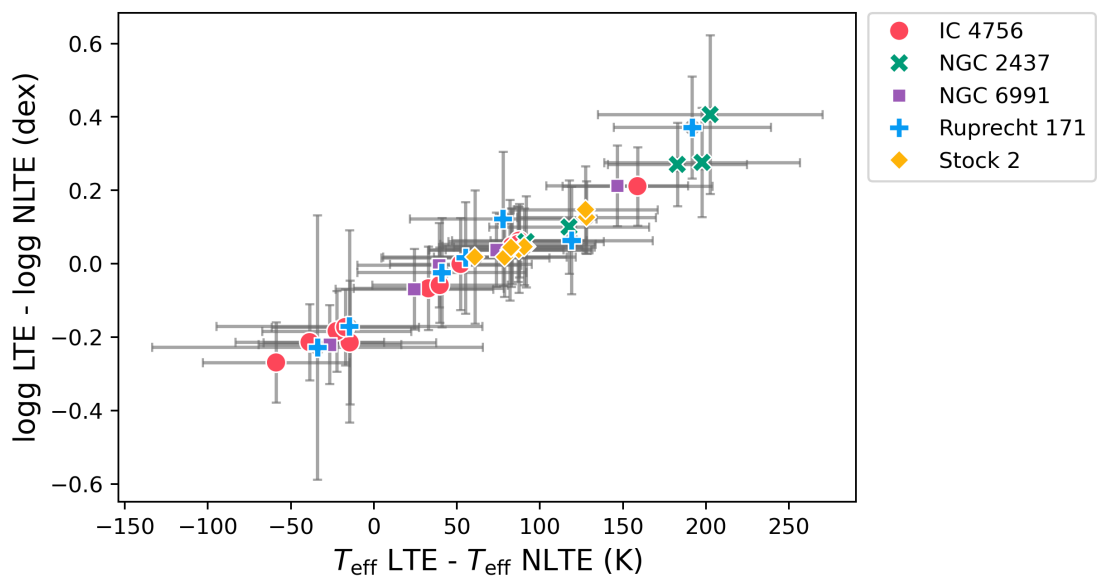
## Appendix A: Properties of the individual stars

**Table A.1.** Properties of the stars of the new open clusters within the SPA project. The table contains information from *Gaia* DR3, exposure times in seconds, resulting S/N, and RV from iSpec.

Name	Gaia DR3 ID	RA	DEC	G	G <sub>BP</sub>	G <sub>RP</sub>	Exp.T	S/N	RV <sub>Gaia</sub>	RV <sub>spec</sub>
<b>IC 4756</b>										
#0	4283940671842998272	279.682	5.239	9.05	9.60	8.35	3600	92	-25.29 ± 0.15	-25.66 ± 0.02
#2	4283984931511649792	279.399	5.260	7.52	8.25	6.69	690	148	-25.08 ± 0.12	-25.10 ± 0.01
#4	4283901746580386816	279.138	5.212	8.49	9.23	7.65	2100	125	-24.98 ± 0.13	-25.04 ± 0.01
#5	4283961979205354496	280.077	5.314	8.90	9.48	8.18	2100	174	-24.98 ± 0.15	-25.31 ± 0.01
#7	4284658038773033728	278.948	5.338	9.10	9.73	8.33	1380	121	-25.00 ± 0.22	-25.15 ± 0.01
#8	4283900062953084800	279.158	5.136	9.10	9.73	8.33	1380	133	-27.75 ± 0.34	-27.23 ± 0.01
#9	4284802074805175936	279.621	5.981	9.13	9.67	8.44	1400	90	-25.21 ± 0.22	-25.61 ± 0.02
#11	4283789905627894272	278.891	4.450	9.42	10.04	8.66	1800	92	-25.07 ± 0.32	-25.13 ± 0.02
#12	4283983552796484864	279.376	5.204	9.44	10.02	8.70	1800	86	–	-25.88 ± 0.02
#13	4284806438475643776	279.337	5.895	9.17	9.67	8.44	1800	115	-24.50 ± 0.14	-24.75 ± 0.02
#14	4283997575895463680	279.272	5.292	9.41	10.00	8.67	1800	115	-25.18 ± 0.16	-25.73 ± 0.01
#15	4286303114338968448	279.851	6.122	8.71	9.28	7.98	1200	110	-25.56 ± 0.13	-25.50 ± 0.01
<b>NGC 2632</b>										
#1	661271173693364864	129.961	19.540	6.39	6.82	5.72	600	188	35.44 ± 0.14	35.31 ± 0.01
HD 73665	661324431287688448	130.026	20.007	6.15	6.62	5.52	1800	144	33.92 ± 0.13	33.97 ± 0.01
<b>NGC 6800</b>										
#1	2023140603917404416	291.570	25.157	10.27	10.94	9.48	3600	71	-14.15 ± 0.21	-14.34 ± 0.02
<b>NGC 6991</b>										
#4	2166845227448342400	313.989	47.395	9.39	9.90	8.73	2800	95	-11.68 ± 0.21	-12.02 ± 0.01
#6	2167008230043576192	313.951	47.910	9.54	10.08	8.85	2800	85	-12.64 ± 0.15	-12.76 ± 0.01
#7	2166853228954093312	313.542	47.382	9.60	10.11	8.92	2800	86	–	-12.42 ± 0.01
#9	2166908105771609472	313.348	47.670	9.76	10.30	9.06	2800	75	-12.87 ± 0.13	-12.95 ± 0.01
#10	2166821789793563904	313.462	47.085	9.81	10.38	9.10	2800	87	-12.44 ± 0.18	-12.65 ± 0.01
<b>NGC 7086</b>										
#1	2171663253032105984	322.486	51.223	9.73	10.65	8.80	1400	79	-22.06 ± 0.17	-22.09 ± 0.02
#2	2171707542735344000	322.589	51.610	9.44	10.54	8.41	2800	89	-20.60 ± 0.13	-20.32 ± 0.02
<b>NGC 752</b>										
#3	342937195667536512	29.263	38.134	8.65	9.15	7.99	2100	228	5.76 ± 0.15	5.38 ± 0.01
#4	342899537393760512	29.812	38.015	8.73	9.23	8.07	2100	194	4.86 ± 0.15	4.75 ± 0.01
#5	342890127122193280	29.720	37.816	8.78	9.30	8.11	2100	230	5.93 ± 0.16	5.86 ± 0.01
#6	344569012659424512	31.304	39.396	9.17	9.62	8.55	1500	160	-4.90 ± 0.20	-5.03 ± 0.02
#7	325299727783639552	35.419	33.476	9.29	9.85	8.58	2100	162	52.46 ± 0.18	52.15 ± 0.01
<b>UBC 3</b>										
#1	4505874693061489280	283.793	12.329	10.02	10.82	9.14	3600	83	1.92 ± 0.18	2.09 ± 0.02
<b>UBC 60</b>										
#3	179623851673246464	67.885	39.370	10.11	10.87	9.26	3000	98	-6.18 ± 0.17	-6.08 ± 0.02
<b>UBC 131</b>										
#1	1814336194629117824	310.234	20.027	10.25	10.75	9.59	4200	90	23.89 ± 0.19	23.88 ± 0.01
#2	1817359031271791232	310.261	20.482	10.66	11.16	10.01	4200	73	23.66 ± 0.20	23.71 ± 0.01
#3	1814243324558277248	310.049	19.942	10.71	11.20	10.06	4200	63	24.32 ± 0.22	24.19 ± 0.02
<b>UBC 141</b>										
#1	1869885794120648192	313.475	35.695	11.51	12.22	10.68	4830	43	-18.43 ± 0.23	-18.59 ± 0.01
<b>UBC 169</b>										
#1	1988520659206227840	342.615	49.468	9.75	10.33	9.03	2800	76	-30.02 ± 0.15	-30.13 ± 0.03
#2	1988520899724392064	342.671	49.518	9.74	10.31	9.03	2800	74	-29.74 ± 0.15	-29.85 ± 0.04
<b>UBC 170</b>										
#1	2007935075311695872	337.878	58.021	10.16	10.98	9.27	4200	86	-28.40 ± 0.16	-28.59 ± 0.03
#2	2007981499630067456	337.770	58.042	10.42	11.23	9.53	4200	72	-28.50 ± 0.24	-28.41 ± 0.03
#3	2007934044519547904	337.712	57.992	10.42	11.21	9.55	2846	78	-28.51 ± 0.17	-28.84 ± 0.02
<b>UBC 194</b>										
#1	354343808469156608	37.709	48.284	9.63	10.22	8.89	3600	131	-29.85 ± 0.18	-30.12 ± 0.04
<b>UBC 577</b>										
#1	4531532690223665664	282.260	22.216	11.07	11.64	10.34	4830	35	-9.04 ± 0.17	-9.33 ± 0.01
#2	4531526058785223424	282.158	22.124	11.28	11.87	10.55	4830	58	-8.90 ± 0.19	-9.06 ± 0.01
#3	4531525337240008576	282.118	22.059	10.36	10.94	9.63	5400	74	-9.24 ± 0.14	-9.55 ± 0.02
#5	4531474038155634560	281.974	21.654	11.02	11.57	10.31	4200	45	-9.26 ± 0.19	-9.34 ± 0.01

**Appendix B: LOTUS Markov-Chain Monte Carlo corner plot**


**Fig. B.1.** Marginalized posterior distributions of the stellar parameters for IC 4756 star #5, with the blue intersecting lines indicating the optimized parameters obtain by LOTUS.

**Appendix C: Comparison of LTE and NLTE atmospheric parameters**


**Fig. C.1.** Differences between LTE and NLTE atmospheric parameters obtained with LOTUS for stars in five open clusters.

## Appendix D: Line list

Table D.1. Line list for the TSFitPy synthesis.

Wavelength (Å)	Ion	E.P. (eV)	log $gf$	Wavelength (Å)	Ion	E.P. (eV)	log $gf$
5688.200	11.01	2.104	-0.404	6554.223	22.01	1.443	-1.150
6154.226	11.01	2.102	-1.547	4911.193	22.02	3.124	-0.640
6160.747	11.01	2.104	-1.246	5418.751	22.02	1.582	-2.130
5711.088	12.01	4.346	-1.742	4761.506	25.01	2.953	-0.548
6696.023	13.01	3.143	-1.569	4765.852	25.01	2.941	-0.445
6698.673	13.01	3.143	-1.870	4813.476	27.01	3.216	-0.191
5675.417	14.01	5.619	-1.234	4867.869	27.01	3.117	-0.193
5684.484	14.01	4.954	-1.607	5369.588	27.01	4.259	-1.174
5701.104	14.01	4.930	-1.981	5483.353	27.01	1.710	-2.234
5772.146	14.01	5.082	-1.643	4829.023	28.01	3.542	-0.140
5793.073	14.01	4.930	-1.894	4913.973	28.01	3.743	-0.500
5948.541	14.01	5.082	-1.230	4935.830	28.01	3.941	-0.213
6555.462	14.01	5.984	-0.886	5748.351	28.01	1.676	-3.240
6721.848	14.01	5.863	-0.940	5805.217	28.01	4.167	-0.579
4758.118	22.01	2.249	0.510	6007.310	28.01	1.676	-3.400
4913.614	22.01	1.873	0.220	6108.116	28.01	1.676	-2.600
4999.503	22.01	0.826	0.320	6128.973	28.01	1.676	-3.430
5016.161	22.01	0.848	-0.480	6175.366	28.01	4.089	-0.389
5024.844	22.01	0.818	-0.530	6482.798	28.01	1.935	-2.630
5866.451	22.01	1.067	-0.790	6586.310	28.01	1.951	-2.780
5953.160	22.01	1.887	-0.273	4607.330	38.01	0.000	0.283
5965.828	22.01	1.879	-0.353	4883.682	39.02	1.084	0.190
5978.541	22.01	1.873	-0.440	4900.119	39.02	1.033	0.030
6261.098	22.01	1.430	-0.530	6645.064	63.02	1.380	-1.814

## Appendix E: Abundance sensitivities

Table E.1. Abundance sensitivities to change in stellar parameters for a sub-sample of stars.

Species	Star	$\Delta T_{\text{eff}}$ (+100 K)	$\Delta \log g$ (+0.2 dex)	$\Delta [\text{Fe}/\text{H}]$ (+0.2 dex)	$\Delta \xi$ (+0.2 km s <sup>-1</sup> )
[Mg/Fe]	IC 4756 #4	0.063	0.005	-0.201	-0.094
	IC 4756 #5	0.062	-0.021	-0.201	-0.073
	IC 4756 #9	0.065	-0.022	-0.196	-0.064
	NGC 752 #3	0.070	-0.012	-0.197	-0.076
	NGC 6800 #1	0.068	-0.006	-0.204	-0.073
[Si/Fe]	IC 4756 #4	-0.007	0.071	-0.254	-0.037
	IC 4756 #5	0.018	0.043	-0.212	-0.046
	IC 4756 #9	0.029	0.062	-0.192	-0.015
	NGC 752 #3	-0.039	0.008	-0.271	-0.095
	NGC 6800 #1	0.003	0.050	-0.221	-0.044
[Ti/Fe]	IC 4756 #4	0.056	-0.015	-0.025	-0.187
	IC 4756 #5	0.043	-0.005	-0.234	-0.183
	IC 4756 #9	0.044	-0.007	-0.373	-0.127
	NGC 752 #3	0.071	-0.041	-0.403	-0.142
	NGC 6800 #1	0.044	-0.028	-0.308	-0.111
[Na/Fe]	IC 4756 #4	0.083	-0.011	-0.210	-0.069
	IC 4756 #5	0.071	-0.019	-0.211	-0.049
	IC 4756 #9	0.069	-0.018	-0.205	-0.042
	NGC 752 #3	0.078	-0.015	-0.211	-0.050
	NGC 6800 #1	0.074	-0.013	-0.220	-0.057
[Al/Fe]	IC 4756 #4	0.074	-0.007	-0.205	-0.033
	IC 4756 #5	0.061	-0.007	-0.211	-0.018
	IC 4756 #9	0.060	-0.005	-0.199	-0.015
	NGC 752 #3	0.068	-0.003	-0.222	-0.019
	NGC 6800 #1	0.064	-0.001	-0.237	-0.019
[Mn/Fe]	IC 4756 #4	0.102	-0.004	-0.194	-0.163
	IC 4756 #5	0.080	-0.016	-0.213	-0.125
	IC 4756 #9	0.089	-0.009	-0.207	-0.101
	NGC 752 #3	0.094	-0.028	-0.212	-0.143
	NGC 6800 #1	0.091	-0.024	-0.213	-0.129
[Co/Fe]	IC 4756 #4	0.039	0.028	-0.176	-0.079
	IC 4756 #5	0.078	0.018	-0.190	-0.040
	IC 4756 #9	0.093	0.019	-0.116	-0.021
	NGC 752 #3	0.069	0.000	-0.185	-0.053
	NGC 6800 #1	0.079	0.002	-0.189	-0.047
[Ni/Fe]	IC 4756 #4	0.089	0.034	-0.212	-0.122
	IC 4756 #5	0.111	-0.004	-0.220	-0.103
	IC 4756 #9	0.110	-0.014	-0.211	-0.09
	NGC 752 #3	0.114	0.001	-0.223	-0.112
	NGC 6800 #1	0.120	-0.018	-0.233	-0.105
[Sr/Fe]	IC 4756 #4	-0.107	-0.258	0.009	-0.439
	IC 4756 #5	-0.044	-0.196	-0.442	-0.290
	IC 4756 #9	-0.030	-0.162	-0.412	-0.244
	NGC 752 #3	-0.066	-0.236	-0.469	-0.335
	NGC 6800 #1	-0.066	-0.227	-0.451	-0.299
[Y/Fe]	IC 4756 #4	0.050	0.087	-0.196	-0.168
	IC 4756 #5	0.060	0.089	-0.129	-0.109
	IC 4756 #9	0.012	0.074	-0.152	-0.148
	NGC 752 #3	0.044	0.076	-0.143	-0.139
	NGC 6800 #1	-0.022	0.074	-0.208	-0.180
[Eu/Fe]	IC 4756 #4	-0.010	0.110	-0.160	-0.020
	IC 4756 #5	-0.010	0.090	-0.140	-0.010
	IC 4756 #9	-0.010	0.080	-0.150	-0.010
	NGC 752 #3	-0.010	0.080	-0.140	-0.010
	NGC 6800 #1	-0.010	0.090	-0.120	-0.020

## Appendix F: Abundance trends

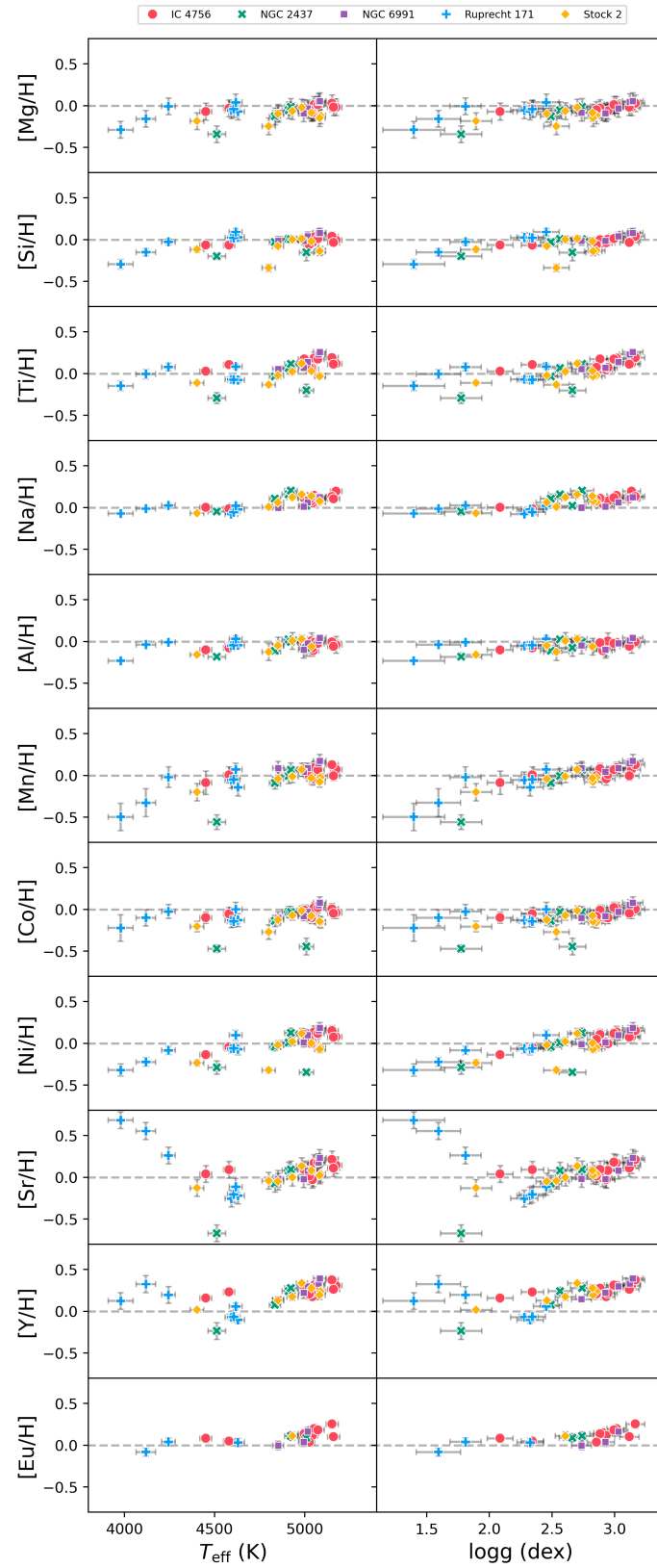


**Fig. F.1.** Abundances  $[X/H]$  as a function of  $T_{\text{eff}}$  (first column) and  $\log g$  (second column). Each symbol represent a different open cluster.

## Appendix G: Comparison with the literature

This table summarizes the comparison with the literature. For  $T_{\text{eff}}$  and  $\log g$  we computed the mean differences (this work - literature) for each OC using the stars in common (N) and the error is the standard deviation. For metallicity and element abundances, we determined the differences by computing the mean cluster abundances derived in this work minus the same from the literature.

**Table G.1.** Differences of the atmospheric parameters and abundances for the OCs in common with the literature.

OC	$T_{\text{eff}}$ (K)	$\log g$ (dex)	N	[Fe/H]	[Mg/Fe]	[Si/Fe]	[Ti/Fe]	[Na/Fe]	[Al/Fe]	[Mn/Fe]	[Co/Fe]	[Ni/Fe]	[Sr/Fe]	[Y/Fe]	[Eu/Fe]	Reference	
<b>New in SPA</b>																	
IC 4756	8 ± 84	0.58 ± 0.24	2	0.15	-	-0.36	-	-0.48	-0.34	-	-	-0.03	-	-	-	Jacobson et al. (2007)	
	-69 ± 5	0.00 ± 0.01	2	-0.03	-	-	-	-	-	-	-	-	-	-	-	Santos et al. (2009)	
	-	-	-	-0.04	0.02	-0.08	0.15	0.10	-	-	-0.11	0.06	-	-	-	-	Smiljanic et al. (2009)
	-65 ± 12	0.01 ± 0.08	2	-0.08	-	-0.12	0.00	-0.10	-0.02	-	-	0.01	-	-	-	Pace et al. (2010)	
	-138 ± 90	-0.49 ± 0.34	6	0.01	-0.15	-	-	-0.12	-0.17	-	-	-	-	-	-	Ting et al. (2012)	
	-48 ± 46	0.27 ± 0.11	8	0.02	-0.11	-0.06	0.10	-0.05	-0.09	0.10	-0.01	0.11	-	0.22	0.05	Bagdonas et al. (2018)	
	-71 ± 87	-0.09 ± 0.20	4	-0.00	0.01	-0.02	0.07	-	-	-	-	0.08	-	-	-	Casamiquela et al. (2017, 2019)	
	-	-	-	0.05	-0.05	-0.08	-	-	0.10	-	-	-	-	-	-	-	Ray et al. (2022)
	50 ± 49	0.21 ± 0.11	8	-	-	-	-	-	-	0.10	-	-	-	-	-	-	Tsantaki et al. (2023)
	-43 ± 35	0.05 ± 0.09	4	0.03	0.02	-0.07	0.11	-0.06	-0.09	0.17	-0.01	0.09	-0.15	0.20	-	-	Carbajo-Hijarrubia et al. (2024)
NGC 6991	-	-	-	0.03	0.01	-0.04	0.15	-0.07	-0.14	0.08	-0.06	0.07	-	0.15	-0.07	Reddy & Lambert (2019)	
	10	0.27	1	0.03	-0.04	-0.02	0.07	-	-	-	-	0.09	-	-	-	Casamiquela et al. (2017, 2019)	
	-	-	-	-0.07	-0.02	-0.06	0.10	-0.11	-0.12	0.15	-0.03	0.06	-0.16	0.16	-	-	Carbajo-Hijarrubia et al. (2024)
NGC 752	-	-	-	0.01	-	-	-	-	-	-	-	-	-	-	-	Sestito et al. (2004)	
	87	-0.29	1	-0.06	-0.17	-0.01	0.14	-0.01	0.05	-	-0.05	0.06	-	0.24	-	-	Carrera & Pancino (2011)
	59 ± 31	0.36 ± 0.08	2	0.06	-0.04	-0.10	0.16	-0.12	-0.22	0.18	-0.02	0.06	-	0.18	0.01	Reddy et al. (2012)	
	67 ± 47	0.36 ± 0.12	3	0.01	0.04	-0.10	0.15	-0.05	-0.10	0.28	0.08	0.03	-	0.27	0.03	Böcek Topcu et al. (2015)	
	29 ± 10	0.13 ± 0.01	2	0.01	-0.03	-0.01	0.07	-	-	-	-	-	-	-	-	Casamiquela et al. (2017, 2019)	
	-91 ± 31	0.31 ± 0.06	2	0.03	-0.09	-0.06	0.01	0.09	-0.27	0.06	-0.15	0.07	-	0.19	-	-	Lum & Boesgaard (2019)
	-	-	-	0.06	0.04	0.04	0.17	-0.05	-0.11	0.05	0.10	0.05	-	-	-	-	Spina et al. (2021)
	-	-	-	0.08	-0.05	0.02	0.15	-0.11	-0.09	0.01	0.02	0.08	-	-	-	-	Myers et al. (2022)
	-	-	-	0.06	0.04	0.03	0.17	-0.04	-0.02	0.03	0.07	0.08	-	-	-	-	Donor et al. (2020)
	-8 ± 11	0.17 ± 0.05	2	0.04	-0.01	-0.05	0.09	-0.10	-0.14	0.14	-0.01	0.08	-0.09	0.18	-	-	Carbajo-Hijarrubia et al. (2024)
UBC 3	-73	0.23	1	0.01	-0.11	-0.18	0.02	-0.15	-0.09	0.04	-0.10	-0.00	-0.26	0.11	-	-	Carbajo-Hijarrubia et al. (2024)
<b>SPA previous studies</b>																	
Collinder 350	55 ± 59	0.26 ± 0.06	2	0.00	-0.13	-0.08	-0.05	-0.16	0.03	-	-0.07	-0.07	-	0.25	0.23	-	
	10 ± 174	0.22 ± 0.21	-	-0.03	-	-	-	-	-	-	-	-	-	-	-	-	
Gulliver 51	156	-0.31	1	-0.09	-0.10	0.04	0.05	-0.13	-0.11	-	-0.06	0.00	-	0.02	0.03	Casali et al. (2020a)	
	66	-0.52	-	-0.014	-	-	-	-	-	-	-	-	-	-	-	-	
NGC 7044	-34 ± 83	0.14 ± 0.14	4	-	-	-	-	-	-	-	-	-	-	-	-	-	
Ruprecht 171	28 ± 73	-0.25 ± 0.09	-	-0.05	-	-	-	-	-	-	-	-	-	-	-	-	
	-136 ± 131	-0.22 ± 0.32	7	-0.13	-0.03	0.00	0.02	-0.09	0.00	-	-0.13	-0.05	-	0.13	0.10	-	
-25 ± 113	-0.24 ± 0.14	-	-0.10	-	-	-	-	-	-	-	-	-	-	-	-		
Alessi 1	-166 ± 125	-0.23 ± 0.31	4	-0.01	0.11	-0.14	0.15	0.12	0.11	-	-	-	-	-	-	-	
Alessi Teutsch 11	-43	0.051	1	0.15	0.07	-0.25	0.15	-0.12	0.02	-	-	-	-	-	-	-	
Basel 11 b	-211 ± 20	-0.45 ± 0.18	3	0.04	0.08	-0.17	0.05	0.00	0.07	-	-	-	-	-	-	-	
COIN-Gaia 30	-404	-0.99	1	-0.07	0.11	-0.09	-0.08	-0.04	0.06	-	-	-	-	-	-	-	
Collinder 350	-60 ± 80	0.13 ± 0.31	2	0.16	-0.10	-0.10	-0.05	-0.07	0.01	-	-	-	-	-	-	-	
Collinder 463	-134 ± 54	-0.20 ± 0.13	2	0.09	0.07	-0.18	0.11	-0.05	0.06	-	-	-	-	-	-	-	
Gulliver 18	-401	-0.98	1	0.09	0.22	-0.21	-0.16	-0.05	-0.14	-	-	-	-	-	-	-	
Gulliver 24	-191	-0.73	1	0.04	0.19	-0.29	0.02	0.08	-0.02	-	-	-	-	-	-	-	
NGC 2437	-184 ± 80	-0.34 ± 0.17	5	-0.03	0.10	-0.16	0.07	0.06	-0.00	-	-	-	-	-	-	Zhang et al. (2021, 2022)	
NGC 2509	68	0.35	1	0.31	0.06	-0.17	0.18	-0.09	-0.08	-	-	-	-	-	-	-	
NGC 2548	-156 ± 149	-0.22 ± 0.46	3	0.07	0.10	-0.06	0.06	0.08	0.07	-	-	-	-	-	-	-	
NGC 2682	-71 ± 157	0.03 ± 0.30	2	0.05	0.05	-0.06	0.19	0.04	0.05	-	-	-	-	-	-	-	
NGC 7209	-168	0.37	1	0.01	0.07	-0.15	0.04	0.17	-0.00	-	-	-	-	-	-	-	
Tombaugh 5	-197 ± 223	-0.44 ± 0.56 ± 3	3	0.00	0.08	-0.16	-0.05	-0.11	0.10	-	-	-	-	-	-	-	
UPK 219	-290	-0.54	1	0.05	0.05	-0.20	-0.09	-0.23	0.00	-	-	-	-	-	-	-	
Stock 2	-42 ± 238	-0.23 ± 0.37	8	0.05	0.10	-0.13	0.06	-0.05	0.09	0.04	-0.12	-0.01	-0.06	0.01	-	Alonso-Santiago et al. (2021)	
<b>Literature</b>																	
Basel 11b	-	-	-	0.04	-0.04	-0.09	0.06	0.03	0.06	-0.11	-0.02	0.01	-	-	-	Donor et al. (2020)	
	-	-	-	0.07	0.02	-0.07	0.06	-0.06	-0.01	-0.14	0.02	-0.02	-	-	-	Spina et al. (2021)	
Collinder 350	36	0.09	1	-0.14	-0.13	-0.12	0.07	-	-0.04	-	-0.03	0.02	-	0.24	0.18	Pakhomov et al. (2009)	
	-	-	-	0.07	-0.16	-0.15	-0.07	-	-	-	-0.08	-0.07	-	0.11	-	Blanco-Cuaresma et al. (2015)	
Stock 2	-	-	-	-0.06	-0.01	0.02	-0.03	-	-	-	0.01	-0.03	-	0.11	0.18	Blanco-Cuaresma & Fraix-Burnet (2018)	
	36 ± 68	0.31 ± 0.13	2	0.04	-0.13	-0.17	0.07	-0.18	-0.10	0.04	-0.10	-0.02	-	0.22	0.01	Reddy & Lambert (2019)	
NGC 2548	102	-1.96	1	-	-	-	-	-	-	-	-	-	-	-	-	Sun et al. (2020)	
	-24	0.17	1	0.04	-0.01	0.00	-0.03	-0.11	-0.11	-0.02	-0.06	-0.05	-	0.26	0.11	Spina et al. (2021)	
NGC 2632	-	-	-	0.03	0.07	0.07	0.08	0.20	-0.05	0.06	0.08	0.12	-	0.08	-	Spina et al. (2021)	
	-144 ± 69	-0.12 ± 0.17	2	-0.07	0.01	-0.03	0.08	-0.06	-0.18	0.16	-0.07	0.05	-0.19	0.05	-	Carbajo-Hijarrubia et al. (2024)	
NGC 2682	-	-	-	0.07	-0.07	-0.07	0.10	-0.13	-0.13	-	-0.06	0.05	-	-	-	Tautvaišiene et al. (2000)	
	-	-	-	0.02	-0.13	-0.06	0.02	-0.24	-0.16	-	-	0.01	-	-	-	Yong et al. (2006)	
	-	-	-	-0.01	-0.24	-0.07	0.18	-0.02	-0.02	-	-0.06	0.04	-	0.14	-	Pancino et al. (2010)	
	-	-	-	0.01	-0.02	-0.15	0.28	-0.07	-0.10	-	0.18	0.11	-	-	-	Friel et al. (2010)	
	22 ± 6	0.15 ± 0.09	2	0.05	-0.20	-0.18	0.24	0.03	-	-	-	0.10	-	-	-	Jacobson et al. (2011)	
	-87 ± 28	0.01 ± 0.08	2	0.08	0.03	0.01	-	0.03	-0.00	-	-	-	-	-	-	Gao et al. (2018)	
	-32 ± 18	0.04 ± 0.02	2	0.01	0.02	-0.02	0.10	-	-	-	-	0.03	-	-	-	Casamiquela et al. (2017, 2019)	
	-	-	-	0.04	0.03	0.02	0.14	0.01	-0.03	0.02	-0.28	0.10	-	0.06	0.04	Spina et al. (2021)	
	-	-	-	0.03	0.03	0.03	0.15	0.02	0.02	0.02	0.04	0.07	-	-	-	Donor et al. (2020)	
	-94 ± 14	0.01 ± 0.01	2	0.01	0.02	-0.08	0.10	-0.15	-0.14	0.11	-0.03	0.02	-0.12	0.16	-	Carbajo-Hijarrubia et al. (2024)	
Ruprecht 171	-220 ± 36	-0.20 ± 0.08	3	-0.22	0.01	-0.02	0.02	-0.10	-0.13	0.03	-0.02	-0.07	0.07	0.15	-	Carbajo-Hijarrubia et al. (2024)	
Tombaugh 5	25	0.27	1	-0.04	-	-0.07	-0.07	-	-	-	-0.10	-	-	-	-	Baratella et al. (2018)	

**Notes:** For the Casali et al. (2020a), the first difference value in  $T_{\text{eff}}$ ,  $\log g$  and [Fe/H] is related to FAMA and the second to ROTFIT results.

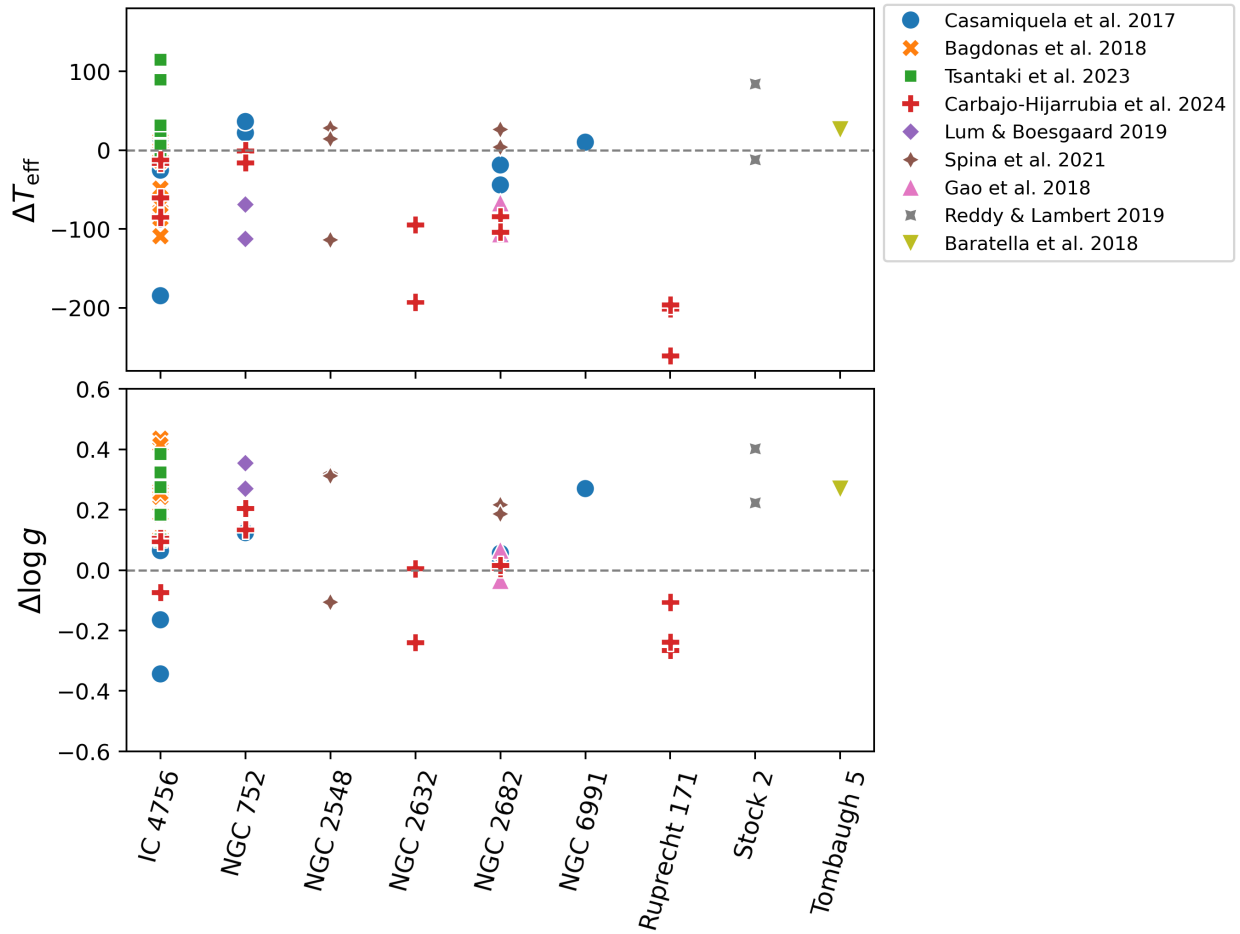


**Fig. G.1.** Comparison of atmospheric parameters for stars matched with the literature, showing star-by-star differences.

## Appendix H: GALAH DR3 open clusters

Table H.1. Open clusters selected from Spina et al. (2021) with mean abundances exclusively from GALAH DR3.

Cluster	[Fe/H]	[Mg/Fe]	[Si/Fe]	[Ti/Fe]	[Na/Fe]	[Al/Fe]	[Mn/Fe]	[Co/Fe]	[Ni/Fe]	[Sr/Fe]	[Y/Fe]	[Eu/Fe]
ASCC 16	-0.369 ± 0.24	-0.066 ± 0.10	0.161 ± 0.21	-0.040 ± 0.04	0.165 ± 0.12	0.029 ± 0.01	0.089 ± 0.14	-	-0.019 ± 0.01	-	0.341 ± 0.11	-
ASCC 19	0.413 ± 0.41	-0.049 ± 0.00	-0.033 ± 0.01	-0.122 ± 0.01	-0.048 ± 0.01	-0.054 ± 0.01	0.101 ± 0.00	-	-0.213 ± 0.01	-	0.533 ± 0.01	-
ASCC 99	0.152 ± 0.10	-0.151 ± 0.15	-0.081 ± 0.10	-0.106 ± 0.14	-0.089 ± 0.10	-0.148 ± 0.11	-0.060 ± 0.15	0.227 ± 0.21	-0.060 ± 0.17	-	-0.057 ± 0.23	-
Alessi 9	-0.065 ± 0.12	-0.051 ± 0.07	-0.076 ± 0.06	0.188 ± 0.19	-0.164 ± 0.13	0.001 ± 0.01	-0.073 ± 0.03	-0.206 ± 0.01	-0.141 ± 0.01	-	0.337 ± 0.14	-
Alessi 24	-0.137 ± 0.20	-0.109 ± 0.06	-0.030 ± 0.07	0.006 ± 0.04	-0.005 ± 0.10	-0.035 ± 0.07	-0.059 ± 0.12	0.097 ± 0.14	-0.042 ± 0.07	-	0.163 ± 0.24	-
Berkeley 32	-0.484 ± 0.14	0.050 ± 0.18	0.280 ± 0.20	0.176 ± 0.12	0.269 ± 0.21	0.200 ± 0.06	0.135 ± 0.19	-0.026 ± 0.06	0.068 ± 0.15	-	-0.018 ± 0.20	0.079 ± 0.08
Berkeley 33	-0.213 ± 0.10	-0.037 ± 0.14	-0.043 ± 0.09	0.291 ± 0.16	0.211 ± 0.09	0.070 ± 0.10	-0.166 ± 0.14	-	-0.081 ± 0.11	0.806 ± 0.20	0.401 ± 0.21	-0.169 ± 0.12
Berkeley 73	-0.410 ± 0.14	-0.070 ± 0.06	0.085 ± 0.04	0.437 ± 0.41	0.143 ± 0.08	0.314 ± 0.23	-0.084 ± 0.06	-0.102 ± 0.01	0.490 ± 0.33	0.866 ± 0.01	0.210 ± 0.01	0.589 ± 0.24
BH 99	-0.150 ± 0.01	-0.072 ± 0.01	0.088 ± 0.03	-	0.052 ± 0.01	-0.045 ± 0.04	-0.007 ± 0.02	-	-	-	0.035 ± 0.05	-
Blanco 1	-0.054 ± 0.08	-0.019 ± 0.10	-0.038 ± 0.09	0.004 ± 0.12	-0.114 ± 0.09	-0.047 ± 0.07	-0.033 ± 0.09	0.138 ± 0.20	-0.068 ± 0.09	0.661 ± 0.01	0.198 ± 0.16	-
Collinder 69	-0.126 ± 0.22	-0.075 ± 0.16	0.016 ± 0.13	-0.031 ± 0.10	0.025 ± 0.17	0.072 ± 0.15	0.046 ± 0.11	-0.264 ± 0.01	-0.067 ± 0.20	-	-0.033 ± 0.11	0.142 ± 0.01
Collinder 135	-0.032 ± 0.05	-0.054 ± 0.08	-0.056 ± 0.05	0.043 ± 0.07	-0.075 ± 0.07	-0.014 ± 0.05	-0.007 ± 0.06	0.233 ± 0.01	-0.136 ± 0.05	-	0.172 ± 0.14	-
Collinder 261	-0.048 ± 0.12	-0.087 ± 0.19	0.025 ± 0.10	-0.006 ± 0.18	0.034 ± 0.14	0.064 ± 0.13	-0.086 ± 0.26	-0.015 ± 0.16	0.011 ± 0.16	0.426 ± 0.23	-0.023 ± 0.31	0.109 ± 0.16
Collinder 359	-0.077 ± 0.10	-0.105 ± 0.07	0.096 ± 0.14	-0.038 ± 0.01	0.164 ± 0.12	0.027 ± 0.10	0.135 ± 0.12	-	-0.003 ± 0.01	-	0.094 ± 0.01	-
Gulliver 6	-0.006 ± 0.22	-0.115 ± 0.12	0.089 ± 0.17	0.024 ± 0.10	-0.048 ± 0.12	-0.116 ± 0.11	0.042 ± 0.19	-	-0.150 ± 0.04	-	0.165 ± 0.25	-
Gulliver 13	-0.249 ± 0.06	0.101 ± 0.01	0.008 ± 0.01	0.344 ± 0.01	0.344 ± 0.01	0.027 ± 0.01	-0.233 ± 0.01	-	-	-	0.282 ± 0.01	-
IC 2602	-0.140 ± 0.17	-0.014 ± 0.05	-0.005 ± 0.05	-0.007 ± 0.08	0.025 ± 0.12	0.006 ± 0.10	0.053 ± 0.05	-0.210 ± 0.01	0.055 ± 0.11	-	0.179 ± 0.11	-
IC 4665	-0.134 ± 0.22	-0.072 ± 0.10	-0.019 ± 0.08	-0.035 ± 0.07	0.048 ± 0.18	-0.017 ± 0.06	0.083 ± 0.08	-	-0.172 ± 0.05	-	0.281 ± 0.17	-
LP 5	-0.123 ± 0.01	0.098 ± 0.23	0.207 ± 0.07	-	0.232 ± 0.03	0.022 ± 0.01	0.351 ± 0.30	-0.254 ± 0.01	-0.011 ± 0.01	-	-0.072 ± 0.01	-
Mamajek 4	0.001 ± 0.14	-0.102 ± 0.14	0.024 ± 0.09	0.069 ± 0.18	0.042 ± 0.13	-0.011 ± 0.10	0.012 ± 0.09	0.154 ± 0.16	-0.016 ± 0.10	-	0.148 ± 0.26	-
Melotte 22	-0.034 ± 0.15	-0.033 ± 0.10	-0.032 ± 0.09	0.030 ± 0.12	-0.008 ± 0.13	-0.033 ± 0.07	0.020 ± 0.08	0.139 ± 0.26	-0.075 ± 0.22	0.182 ± 0.01	0.194 ± 0.12	-
Melotte 25	0.120 ± 0.18	-0.048 ± 0.18	-0.119 ± 0.12	0.041 ± 0.14	0.048 ± 0.24	0.025 ± 0.08	0.049 ± 0.17	-0.048 ± 0.13	-0.022 ± 0.19	-	0.299 ± 0.33	-
Melotte 101	-0.154 ± 0.01	0.123 ± 0.01	0.057 ± 0.01	-0.014 ± 0.01	0.350 ± 0.01	0.206 ± 0.01	0.057 ± 0.01	-0.001 ± 0.01	0.125 ± 0.01	-	0.427 ± 0.01	0.013 ± 0.01
NGC 1647	0.174 ± 0.01	-0.209 ± 0.01	-0.110 ± 0.01	-	-0.205 ± 0.01	-	-	-	-	-	-	-
NGC 1750	-0.337 ± 0.14	-0.182 ± 0.20	0.061 ± 0.16	-	0.170 ± 0.09	-	0.071 ± 0.04	-	-	-	0.500 ± 0.17	-
NGC 1817	-0.088 ± 0.11	-0.068 ± 0.10	0.026 ± 0.12	0.011 ± 0.12	0.174 ± 0.11	-0.007 ± 0.08	-0.026 ± 0.12	-0.106 ± 0.12	0.042 ± 0.12	-	0.122 ± 0.21	0.010 ± 0.13
NGC 1901	-0.272 ± 0.25	-0.119 ± 0.14	0.014 ± 0.09	0.100 ± 0.12	0.066 ± 0.11	-0.054 ± 0.10	-0.045 ± 0.12	-	-0.167 ± 0.01	-	0.197 ± 0.22	-
NGC 2112	-0.083 ± 0.08	-0.000 ± 0.11	-0.025 ± 0.09	0.045 ± 0.17	-0.008 ± 0.12	0.023 ± 0.15	-0.006 ± 0.12	-0.062 ± 0.11	-0.019 ± 0.09	-	0.010 ± 0.32	0.016 ± 0.10
NGC 2204	-0.325 ± 0.09	-0.003 ± 0.07	0.043 ± 0.10	0.069 ± 0.11	0.242 ± 0.14	0.075 ± 0.12	-0.019 ± 0.15	-0.037 ± 0.09	-0.007 ± 0.09	0.916 ± 0.01	0.227 ± 0.44	0.088 ± 0.08
NGC 2215	-0.100 ± 0.06	0.117 ± 0.06	0.022 ± 0.05	-0.010 ± 0.05	0.010 ± 0.04	-0.121 ± 0.06	-0.009 ± 0.06	-	-0.127 ± 0.07	-	0.004 ± 0.10	-
NGC 2232	-0.238 ± 0.19	-0.048 ± 0.15	0.074 ± 0.06	0.040 ± 0.05	0.127 ± 0.11	0.069 ± 0.08	0.038 ± 0.09	0.775 ± 0.01	-0.011 ± 0.11	-	0.254 ± 0.27	-
NGC 2243	-0.340 ± 0.12	-0.027 ± 0.14	0.010 ± 0.11	0.117 ± 0.12	0.227 ± 0.07	0.022 ± 0.14	0.074 ± 0.18	-0.088 ± 0.05	0.025 ± 0.13	-	0.039 ± 0.22	0.285 ± 0.06
NGC 2318	0.002 ± 0.20	-	-	-	0.649 ± 0.10	-	0.134 ± 0.14	-	-	-	-	-
NGC 2506	-0.173 ± 0.12	-0.071 ± 0.21	-0.134 ± 0.12	0.214 ± 0.09	0.247 ± 0.12	-0.007 ± 0.12	0.341 ± 0.20	-0.087 ± 0.10	0.008 ± 0.14	-	0.288 ± 0.29	0.241 ± 0.14
NGC 2516	-0.137 ± 0.29	-0.079 ± 0.12	-0.004 ± 0.13	-0.002 ± 0.12	-0.082 ± 0.22	-0.082 ± 0.09	-0.009 ± 0.12	0.110 ± 0.25	-0.101 ± 0.16	-	0.240 ± 0.25	-
NGC 2539	0.023 ± 0.28	-0.158 ± 0.09	-0.101 ± 0.08	-0.014 ± 0.08	0.095 ± 0.12	-0.018 ± 0.06	-0.107 ± 0.14	-0.131 ± 0.14	0.009 ± 0.11	-	0.209 ± 0.23	-0.040 ± 0.12
NGC 2548	-0.241 ± 0.26	-0.045 ± 0.02	-0.002 ± 0.02	-0.018 ± 0.04	0.290 ± 0.11	0.053 ± 0.02	0.090 ± 0.28	-0.068 ± 0.04	0.075 ± 0.04	-	0.546 ± 0.15	-0.031 ± 0.03
NGC 2632	0.198 ± 0.13	-0.076 ± 0.09	-0.057 ± 0.13	-0.035 ± 0.08	-0.006 ± 0.11	-0.009 ± 0.08	0.051 ± 0.10	0.031 ± 0.22	-0.010 ± 0.10	0.531 ± 0.18	0.090 ± 0.21	-
NGC 2682	-0.046 ± 0.16	0.016 ± 0.13	0.018 ± 0.14	0.055 ± 0.14	0.048 ± 0.12	0.030 ± 0.14	0.030 ± 0.16	0.319 ± 0.31	0.035 ± 0.12	0.548 ± 0.03	0.028 ± 0.21	0.013 ± 0.06
NGC 3680	-0.263 ± 0.07	-0.283 ± 0.01	0.299 ± 0.01	-	0.172 ± 0.03	-	0.063 ± 0.01	-	-	-	0.329 ± 0.01	-
NGC 5460	-0.402 ± 0.01	-	-	-	0.273 ± 0.01	-	-	-	-	-	-	-
NGC 6253	0.159 ± 0.14	0.048 ± 0.10	0.115 ± 0.14	0.078 ± 0.18	0.308 ± 0.13	0.191 ± 0.19	0.205 ± 0.13	0.219 ± 0.10	0.159 ± 0.13	0.458 ± 0.32	0.015 ± 0.15	-0.042 ± 0.05
Ruprecht 145	-0.257 ± 0.26	-0.090 ± 0.06	0.058 ± 0.10	-0.065 ± 0.04	0.256 ± 0.11	0.015 ± 0.05	0.053 ± 0.07	-0.141 ± 0.04	0.015 ± 0.04	-	0.477 ± 0.34	-0.153 ± 0.01
Ruprecht 147	0.025 ± 0.14	-0.038 ± 0.04	-0.009 ± 0.07	0.002 ± 0.08	0.121 ± 0.07	0.051 ± 0.11	0.042 ± 0.10	-0.037 ± 0.03	0.001 ± 0.10	-	0.083 ± 0.10	-0.028 ± 0.05
Trumpler 20	-0.469 ± 0.17	-0.304 ± 0.13	0.124 ± 0.13	0.021 ± 0.37	0.177 ± 0.13	0.443 ± 0.10	-0.796 ± 0.11	0.442 ± 0.23	0.341 ± 0.17	0.733 ± 0.17	-0.752 ± 0.11	0.225 ± 0.14
Trumpler 26	0.190 ± 0.07	-0.017 ± 0.08	0.002 ± 0.06	-0.016 ± 0.05	0.464 ± 0.05	0.189 ± 0.07	0.181 ± 0.08	-0.045 ± 0.06	-	-	0.374 ± 0.16	-0.222 ± 0.10
Turner 5	-0.081 ± 0.07	-0.055 ± 0.08	0.005 ± 0.06	-0.008 ± 0.07	-0.106 ± 0.06	-0.038 ± 0.07	-0.006 ± 0.08	-	-0.062 ± 0.08	-	-0.039 ± 0.14	-
UBC 95	-0.586 ± 0.30	-0.052 ± 0.01	0.034 ± 0.01	-0.357 ± 0.01	0.347 ± 0.01	0.404 ± 0.01	-0.242 ± 0.01	0.248 ± 0.01	0.103 ± 0.01	0.460 ± 0.01	-0.019 ± 0.01	-
UBC 212	-0.272 ± 0.09	-0.139 ± 0.11	0.106 ± 0.08	-0.040 ± 0.10	0.262 ± 0.07	0.103 ± 0.09	-0.097 ± 0.11	-0.049 ± 0.19	-0.169 ± 0.10	-	0.293 ± 0.19	0.243 ± 0.11
UBC 260	-0.345 ± 0.04	-	-	-	0.352 ± 0.01	-	-	-	-	-	0.381 ± 0.01	-
UBC 511	-0.415 ± 0.07	-0.236 ± 0.05	0.147 ± 0.04	-	0.205 ± 0.03	-	0.483 ± 0.04	-	-	-	0.765 ± 0.07	-
UPK 40	0.061 ± 0.09	-0.064 ± 0.01	0.171 ± 0.01	-	0.104 ± 0.07	-	0.027 ± 0.01	-	-	-	-	-
UPK 467	-0.371 ± 0.49	-0.027 ± 0.01	0.036 ± 0.01	-0.008 ± 0.01	0.131 ± 0.01	0.225 ± 0.01	0.091 ± 0.01	0.039 ± 0.01	0.171 ± 0.01	-	-0.129 ± 0.01	-
UPK 524	0.008 ± 0.11	0.015 ± 0.04	-0.015 ± 0.10	0.147 ± 0.01	-0.045 ± 0.01	-0.025 ± 0.14	-0.012 ± 0.01	-	-0.260 ± 0.01	-	0.214 ± 0.22	-
UPK 526	-0.147 ± 0.01	-0.060 ± 0.01	0.026 ± 0.01	0.233 ± 0.01	0.056 ± 0.01	0.174 ± 0.19	-0.055 ± 0.05	-	-	-	0.084 ± 0.07	-
UPK 540	0.269 ± 0.15	-0.481 ± 0.27	-	-	-0.273 ± 0.15	-0.466 ± 0.14	-0.010 ± 0.25	-	0.275 ± 0.23	-	-	-
UPK 545	0.260 ± 0.38	-0.113 ± 0.17	0.144 ± 0.04	0.339 ± 0.01	0.110 ± 0.21	0.061 ± 0.21	-0.009 ± 0.12	-0.077 ± 0.01	-0.557 ± 0.01	-	0.045 ± 0.01	-
UPK 552	-0.528 ± 0.12	-	-	-	-	-	-	-	-	-	0.209 ± 0.19	-
UPK 579	-0.210 ± 0.07	0.009 ± 0.10	0.093 ± 0.07	0.120 ± 0.03	0.149 ± 0.03	0.075 ± 0.08	-0.064 ± 0.10	0.815 ± 0.01	0.080 ± 0.01	-	0.278 ± 0.27	-
UPK 587	-0.557 ± 0.33	-0.214 ± 0.14	0.169 ± 0.01	-	0.347 ± 0.16	0.376 ± 0.01	0.152 ± 0.04	-	-	-	0.421 ± 0.10	-
UPK 599	-0.375 ± 0.25	-0.110 ± 0.01	0.016 ± 0.01	0.325 ± 0.01	0.046 ± 0.01	-0.010 ± 0.01	-0.090 ± 0.01	-	-	-	0.057 ± 0.01	-
UPK 612	-0.060 ± 0.21	-0.097 ± 0.05	-0.070 ± 0.04	-0.025 ± 0.04	-0.061 ± 0.03	0.009 ± 0.19	-0.055 ± 0.08	-	-0.115 ± 0.03	-	0.081 ± 0.05	-
UPK 624	-0.226 ± 0.02	-0.143 ± 0.01	0.108 ± 0.01	-	0.142 ± 0.05	-	-0.100 ± 0.05	-	-	-	0.141 ± 0.05	-